# ELECTRON BEAM MEASUREMENTS OF DENSITY IN SHOCK WAVES REFLECTING FROM A COLD WALL

Thesis by

Hugo de Oliveira Piva

In Partial Fulfillment of the Requirements

For the Degree of

Doctor of Philosophy

California Institute of Technology

Pasadena, California

1968

(Submitted May 17, 1968)

## ACKNOWLEDGMENTS

The author wishes to express his sincere appreciation to Professor Bradford Sturtevant for his guidance and very helpful suggestions throughout the experiments and during the analysis of the results. The author is also very thankful to Professor Hans W. Liepmann for his encouragement in the early part of the experimental work, when great difficulties were encountered. Professor Anatol Roshko deserves very special gratitude for his assistance with both academic and non-academic matters which made it possible for the author and his family to enjoy a much happier life in this country during the years of graduate work.

It is a pleasure to thank Mrs. Geraldine Krentler for typing the manuscript.

The author is indebted to the Brazilian Air Force and Conselho Nacional de Pesquisas (Brazil) for their financial support. The GALCIT 17-in shock tube and the electron-beam densitometer were built under previous NASA contracts.

# ABSTRACT

The normal shock wave is a rarefied-gas flow in which large departures from thermodynamic equilibrium and strong non-linearities occur and it is the simplest such flow due to its one-dimensionality and the absence of solid boundaries. Because of this, both theoretical and experimental studies of the structure of normal shock waves have been used successfully in recent years to get a better understanding of such phenomena. The present work is an extension of the earlier studies to the more complicated problem of shock-wave reflection. The density distribution of a normal shock wave in argon is measured during its reflection from a heat-conducting wall using an electron beam densitometer in the GALCIT 17-in diameter shock tube at incident Mach numbers 6.00, 4.00 and 2.96.

During each run a density history is obtained at a certain distance from the wall by measuring electron-beam current as a function of time. By defining a consistent zero of time for all runs at the same conditions, these histories are converted by a cross-plot to families of density profiles at different times. x-t diagrams are obtained from the density history plots, and a wall-density history is obtained from the density profiles. Measured in terms of the ideal conditions behind the incident shock wave, the distances extend from 0.25 to 56 mean free paths

from the wall and the times to 160 mean collision times after the beginning of the reflection.

The results presented here give both quantitative and qualitative information about the interaction of the incident shock wave with the wall, the effects of the wall heat transfer and accommodation on the density near the wall, the formation of the reflected shock wave, its strength and trajectory on the x-t diagram, and the nature of the flow field lying between the thermal layer and the reflected shock wave at large times.

# TABLE OF CONTENTS

TABLE OF CONTENTS (cont.)

# LIST OF FIGURES

LIST OF FIGURES (cont.)

# I. INTRODUCTION

The normal shock wave is a rarefied-gas flow in which large departures from thermodynamic equilibrium and strong non-linearities occur, and it is the simplest such flow due to its one-dimensionality and the absence of solid boundaries. In view of the present state of understanding of gas-solid interactions, choice of a flow with no solid boundaries has, until now, been necessary in order that the effects of large departures from equilibrium and non-linearities could be studied. In this case the analysis of the experimental results is much easier, and by avoiding hypothetic boundary conditions, the theoretical treatment becomes more realistic. Furthermore, one-dimensional normal shock waves can be accurately produced in the laboratory.

Motivated by the above reasons, much experimental and theoretical work has been done on the structure of normal shock waves in the past few years (e.g., Refs. 1 through 6). As a result of such work important information concerning the behavior of gases when departures from thermodynamic equilibrium are large were obtained, and various theoretical predictions were tested with the experimental data.

The study of the reflection of a normal shock wave from a solid, heat-conducting wall perpendicular to the flow direction is a natural extension of the earlier work to the

more complex problem in which the effects of gas-solid interactions, or accommodation effects, are also important. The present work is an investigation of the density distribution of a normal shock wave in argon during its reflection from a wall using an electron-beam densitometer. The wall is perpendicular to the flow direction to keep the problem one-dimensional and to simplify the velocity boundary conditions (zero velocity at the wall) for comparison with theoretical studies. It has to be heat-conducting for practical reasons and this turns out to be a desirable feature which emphasizes accommodation effects. The convenience of using density as the principal variable will become apparent later.

During the reflection of a shock wave from a heat-conducting wall, three effects are of great importance: 1) the temperature distribution near the wall; 2) formation of the reflected shock and its propagation away from the wall; 3) the nature of the flow between the shock wave and the thermal layer formed near the wall due to heat transfer.

1) A shock wave reflecting from an insulating wall heats the gas between the shock and the wall to very high temperatures. If the wall is heat-conducting it acts like a heat sink, cooling down the gas in its vicinity, but the poor heat-conductivity of the gas restricts this direct influence of the wall to a very thin region, i.e., the lower temperatures are confined to a thin layer near the

wall which grows by diffusion into the rest of the fluid (its thickness increases with the square root of time). The density is higher in this growing thermal layer, and both temperature and density gradients are very steep there. The increasing density requires that mass be supplied, which induces a displacement velocity toward the wall. Thus, the requirement of conservation of mass results in convection of hot gas into the thermal layer, reducing this thickness and, therefore, increasing even more the temperature and density gradients. In addition, the temperature of the gas at the wall ($x = 0+$) is not the same as the temperature of the wall ($x = 0-$), i.e., a temperature jump (thermal slip) occurs at the wall-gas interface, reducing the gradients in the gas. As the thermal slip cannot be directly measured, it has to be studied through its effects in the flow near the wall.

2) The displacement velocity is related to the growth of the dense thermal layer, and the net effect is equivalent to that caused by a receding wall whose speed, according to boundary-layer theory, is inversely proportional to the square root of time. The results of the present experiment indicate that when the incident shock wave hits the wall, the equivalent "receding wall" is set into motion with a very high speed, producing an expansion wave that initially cancels the incoming shock. As the speed of the receding wall decreases, it sends out com-

compression waves into the heated gas. After a short time these compression waves coalesce, forming the reflected shock wave which, in turn becomes stronger and faster as more compression waves overtake it, approaching asymptotically the ideal-shock strength.

3) The nature of the flow field between the reflected shock and the thermal layer for "large times" (large for this experiment) is dominated mainly by both the pressure waves emitted by the thermal layer ("receding wall") and the entropy jump across the shock. The pressure is lower near the shock and increases toward the wall, because near the wall the pressure results from piston motion at later times and is, therefore, more nearly the ideal value. The entropy is higher near the reflected shock and decreases toward the thermal layer, because in the beginning of the reflection process the fluid is processed by a nearly isentropic reflected wave whereas, later on, the shock wave is stronger and the entropy increase across it is larger. The behavior of both pressure and entropy has the same effect on the density distribution, i.e., the density is lower near the shock and increases toward the wall.

The present work reports measurements of density profiles within the reflecting shock layer with sufficient accuracy and resolution that both quantitative and qualitative information can be obtained about the interaction of the incident shock wave with the wall, about the effects of

wall heat transfer and accommodation on the density near the wall, about the formation of the reflected shock wave and its strength and trajectory on the x-t diagram, and about the nature of the flow field lying between the thermal layer and the reflected shock wave at large times.

All of the experiments are performed in argon, and the incident shock Mach numbers M and initial pressures $p_1$ are as follows:

| M | $p_1$ ($\mu$Hg) |
|---|---|
| 6.00 | 15, 35 |
| 4.00 | 15, 50 |
| 2.96 | 50 |

The distances from the wall extend from 0.4 mm to 26 mm (or, measured in terms of conditions behind the incident shock wave, from 0.25 to 56 mean free paths) and the times of 130 $\mu$ sec (160 collision times) after the beginning of the reflection. It should be noted that ionization relaxation is much slower than these time scales and, therefore, ionization at the higher Mach numbers does not affect the present measurements.

# II. EXPERIMENTAL TECHNIQUE

## 2.1 Description of the Equipment

The experiments were performed in the GALCIT 17-in diameter shock tube described in reference 7. The incident-shock speed is obtained by measuring the time interval for the shock to pass between two platinum thin-film heat-transfer gauges (built by Dr. C. Wang and described in Ref. 8) which are 500 mm apart and are centered about a point located 46.6 diameters from the diaphragm. The heat gauges trigger an electronic counter (Hewlett Packard 5233L), which gives the time interval in microseconds. The incident shock Mach number M is defined as the measured speed of the incident shock divided by the speed of sound in the initial gas*.

The electron beam densitometer is the same as that described in reference 3, and figure 1 is a schematic of the equipment. The electron beam is directed across the

---

* The usual shock tube notation will be used throughout this report and is the following:
Region 1 = undisturbed gas ahead of the incident shock wave.
Region 2 = uniform flow behind the incident shock wave.
Region 5 = uniform flow behind the reflected shock wave.
Initial pressure (or temperature, etc.) = pressure (or temperature, etc.) in region 1.
The conditions in regions 2 and 5 are calculated by the Rankine-Hugoniot relations for normal shocks in an ideal gas (Ref. 8) using the measured value of M.

tube, parallel to the end wall at a fixed location 48.5 diameters from the diaphragm. It is produced by a commercial television gun (Superior Electronics S-110E), enters the shock tube through an injector needle and is collected by a small Faraday cage. The needle hole diameter is 0.5 mm and the maximum beam diameter is approximately 0.6 mm. The gap between needle and collector is 12 cm, the accelerating voltage varies from 15 KV to 18 KV, and the beam current varies from 100 μA to 140 μA depending on the initial pressure. However, in every case both voltage and current are kept constant for all runs at the same Mach number and initial pressure.

A movable plate is used for the end wall, and its position with respect to the center of the beam is externally adjusted. It is a 1-in-thick aluminum plate and its reflecting surface had been faced and polished in the lathe. Care has been taken to assure that the plate is parallel to the electron beam and an indication that they are in fact parallel is that a mark left by the beam on the surface of the plate is uniform.

## 2.2 Density Measurement

When the shock wave passes the measuring station the increasing gas density causes an increasing fraction of the electrons to be scattered out of the beam. Therefore, the current collected by the Faraday cage is a measure of the average density of the gas between injector and collector tips. To convert the measured collector current to density the simple attenuation law,

$$\frac{I_o}{I} = \exp(k\rho) \qquad (1)$$

is assumed (Refs. 2 and 3), where $I_o$ is the current through the injector needle, I is the current measured at the collector, $\rho$ is the gas density, and k is the attenuation coefficient. k is a function of the accelerating voltage, grid and focus voltages in the gun, beam collimation, length of the gas sample and the gas properties (e.g., collision cross-section). Thus, it is apparent that the instrument must be calibrated to obtain the values of k for the conditions of the experiment.

The calibration constant k can be determined in three different ways:

a) by a static calibration;

b) since the density in region 1 and the corresponding current (constant current before the arrival of the incident shock) are always known, then, if the current $I_o$

is measured, k can be computed from equation (1) and each run becomes self-calibrating;

c) the density in region 2 is also known and, if the corresponding region can be identified in the current history, then the calibration constant can be obtained by equation (3) below, derived from equation (1). Also the density and current are related to each other and to the conditions in regions 1 and 2 by the formula:

$$\frac{\rho - \rho_1}{\rho_2 - \rho_1} = \frac{\log_e \frac{I_1}{I}}{\log_e \frac{I_1}{I_2}} \tag{2}$$

$$k = \frac{1}{\rho_2 - \rho_1} \log_e \frac{I_1}{I_2} \tag{3}$$

Or, referring to the conditions at $0^{\circ}C$ and 1 atmosphere:

$$\rho_1 = \rho_o \frac{p_1}{p_o} \frac{T_o}{T_1}$$

$$k = \frac{1}{\rho_o} \frac{p_o}{p_1} \frac{T_1}{T_o} \frac{1}{\left(\frac{\rho_2}{\rho_1} - 1\right)} \log_e \frac{I_1}{I_2} \tag{4}$$

p = pressure

T = absolute temperature

The computation of k and the use of the above formulas will be explained in §2.3.2 and §2.3.3.

## 2.3 Experimental Procedure

### 2.3.1 Description of the procedure

For initial pressures of 15 μHg the shock tube is evacuated to 1 μHg, flushed with argon and pumped again to 0.10 μHg before each run. For higher initial pressures it is pumped to 0.10 μHg without flushing. The initial pressure is set with the use of a calibrated container (one thousandth of the volume of the driven section) and a bellows type 0-50 mm Hg Wallace and Tiernan gauge.

The electron beam is then aligned by seeking a position for which the collector current is maximized. The distance between the wall and the center of the beam is measured as follows: the center of the beam is found by moving the end wall toward the beam until the collector current just begins to drop. This point is recorded and the plate is pushed again until the current is zero. The center of the beam is taken to be at the midpoint between those two extremes. To locate the end wall with respect to the center of the beam, the plate is pulled back to approximately 1 mm beyond the desired location and then is pushed again toward the beam to the correct position. A finer alignment of the electron beam is then made by minimizing the ripple observed in the collector current when the recording oscilloscope is set to very high gain. This procedure is repeated before each run. Before the first shot of the day all the electrical adjustments of the

beam are set to the desired positions and are not changed for all subsequent runs.

When the incident shock approaches the measuring station a platinum thin-film heat transfer gauge triggers oscilloscope #1 (dual beam Tektronix type 555). The upper beam displays the collector current and the lower beam measures the injector needle current. The signals in all oscilloscopes are recorded photographically by Polaroid cameras. Oscilloscopes #2 and #3 are single beam Tektronix type 535 and 532, respectively, and are used to record the collector current with a much higher amplification and finer time resolution. The latter is achieved by using scope #1 to trigger the other two after a certain time delay. In scope #2 the density history during the reflection process is expanded to occupy the entire picture, permitting a more accurate reading. This is possible only because of the excellent repeatability of the shock tube conditions, which enables the operator to predict very accurately the speed of the incident shock. Scope #3 uses a less expanded scale, to show the zero in the current trace (see Figs. 2 and 3).

A time-mark generator is used to produce time dots (Ref. 10) at known intervals on the current trace of oscilloscope #2 (Figs. 2 and 3). The sweep-speed of oscilloscope #3 is checked from time to time by means of time dots (Fig. 2).

A short time after the reflection is completed, a pulse of 35 to 50 volts is applied to the deflection plates of the electron gun (Ref. 3) to deflect the beam and determine the zero on the collector current traces. The beam is then turned off automatically and the valve between the shock tube and the electron-gun chamber is closed (also automatically - see Ref. 3).

After the shot a square-wave signal (distorted) is sent simultaneously to all the oscilloscopes and photographed to determine the relative gain of each trace, as shown in figures 2 and 3. The shock tube is then vented with filtered dry air and the diaphragm is changed. During the diaphragm change air is forced by a blower through the dryer into the shock tube until the shock tube is again closed.

2.3.2 Calibration constant k

Referring to the processes described in section 2.2 for finding k, method a) is not used because k is a function of the electrical adjustments of the beam and, since the conditions of the static calibration cannot be reproduced exactly for each run, a scatter of more than $\pm$ 10% in the calibrated density results. With method b) there is still a scatter of 6% due to the inaccuracy in measuring $I_o$ from the oscilloscope traces. By using method c) whenever the measuring station is far enough

from the wall ("large x") to show a plateau in the current trace identifying the uniform region 2 (Fig. 2), the scatter is reduced to less than 3% for shots fired under similar conditions. Also, if the electrical adjustments are the same for similar runs (§ 2.3.1), the values of k computed by equation (4) fall within 3% of the mean value. Therefore, by maintaining the same electrical adjustments, method c) can be extended to the cases where the measurements are too close to the wall ("small x") for there to be a plateau (Fig. 3): the runs at small x are mixed among the ones at large x. The values of k at large x are computed by equation (4) and an average value is obtained for each day. This average is used in the same equation (4) to compute the denominator of the right-hand-side of equation (2), giving:

$$\frac{\rho - \rho_1}{\rho_2 - \rho_1} = \frac{1}{\rho_o} \frac{p_o}{p_1} \frac{T_1}{T_o} \frac{1}{k\left(\frac{\rho_2}{\rho_1} - 1\right)} \log_e \frac{I_1}{I} \qquad (5)$$

2.3.3 Data reduction

The collector current is converted to density by means of equation (2) for large x and equation (5) for small x. The point 2 is defined as the point immediately behind the incident shock wave where, in the plot of current versus time, the curvature disappears and the trace becomes a straight line. This artificial definition

is necessary because, as can be seen in figure 2, the so-called "plateau" is not horizontal probably due to the increase in density behind the incident shock wave caused by the effects of sidewall boundary layers (Ref. 14). The density $\rho_2$ corresponding to point 2 is taken to be the ideal-gas density behind the incoming shock, computed from the Rankine-Hugoniot conditions for normal shocks using the measured values of M. Two typical plots of density versus time are shown in figures 4 and 5. The ordinate is the normalized density: $\rho_1$ is the initial gas density and $\rho_5$ is the ideal-gas density behind the reflected shock wave calculated from the Rankine-Hugoniot conditions using M.

## 2.4 Error Estimate

It was shown in reference 3 that the absolute value of the pressure is known to within 4%, the measurement of the shock Mach number is accurate to 1%, and the shock-speed variation between the last thin-film gauge and the measuring station is less than 1% (Ref. 3). The time marker has an accuracy of 1%. The skewness and curvature of the incident shock have no appreciable influence in this particular set of measurements, as was pointed out in reference 2 based on the results presented in reference 11. The measured Mach numbers have an actual rms variation of 1% for M = 6 and even less for M = 4 and 3. The measured values of M are used in the normalization of density, so the small variations of M are accounted for.

The position of the center of the beam, determined as described in §2.3.1, may vary as much as 0.20 mm for large x (20 mm and up from the wall) from one run to the next, indicating that there is a backlash in the leadscrew system used to move the end wall. This gives an uncertainty of 1% in the measured distances. The normalized times and distances (Sec. 3.1) include the pressure as a factor; therefore, their expected inaccuracies are the sum of the relative error of each factor, i.e., 5% for both time and distance (normalized).

The values of the calibration constant k (§ 2.3.2) vary by 3% (maximum scatter) for runs made on the same day,

probably due to voltage fluctuations in the line, and to errors in the measured values of M, initial pressure and temperature. Therefore the mean values of k used for short distances from the end wall (no plateau in the current trace) and, consequently, the corresponding densities, have an uncertainty of 3%.

The disturbances caused by the interference of the injector needle, the collector cage and the edges of the end plate with the flow may produce spurious effects in the density measurements. After the passage of the incident shock wave, the shocks reflected from the needle and the cage propagate into the region between them, increasing the density of part of the gas sample. The apparent density is further increased by the thermal layer (Chaps. III and IV) developed near the needle and the cage. However, references 2 and 3 report good agreement in the measurements of density profiles in the incident shock obtained for different gaps between needle and cage, indicating that the disturbances caused by them are not important until the incoming shock has passed. On the other hand, any perturbations are amplified by the reflected shock and might become significant after the reflection. For measurements close to the wall, the reflected shock passes the electron beam when the above-described disturbances are just beginning to develop. Therefore, it is expected that their influence is not important for small x. For large x, when the reflected

wave reaches the measuring station the disturbances are fully developed and are already propagating through the gas sample. Therefore, their influence after being amplified by the reflected shock might become important.

The edges of the end plate probably produce expansion waves after the reflection, because they are not sealed, i.e., there is a small gap between the plate and the cookie-cutter (Fig. 1) and also between plate and needle, and plate and cage. The expansion waves coming from the sides never reach the beam during the measurements, but the ones generated by the plate-needle and the plate-cage gaps do reach the beam very quickly, tending to reduce the average density of the gas sample. On the other hand, as described above, the shocks on the needle and cage tend to increase the apparent density. The net effect of such interactions is not known, but in view of the consistency of the results obtained, it is believed that they nearly cancel each other. In fact, for short distances, when the effects of the shocks on the needle and cage are small, the plate-needle and plate-cage gaps are very narrow and the expansion waves originated there (if any) are also very weak. For large x, both effects are stronger.

# III. RESULTS

## 3.1 Density Histories

A density history is obtained at each distance from the wall, as described in §2.3.3. Due to the excellent reproducibility of the shock tube conditions it is possible to obtain a series of such density histories at several distances from the wall, all of them at the same Mach number and initial pressure. Therefore, a set of all those curves can be plotted on the same graph by specifying a consistent origin of time for all of them. In our case t = 0 is chosen to be the instant when the leading edge of the incident shock reaches the wall; the leading edge is defined as the point where the tangent to the point of maximum slope of the incident wave crosses the line of zero normalized density. It is also assumed that the measured shock speed remains constant from the moment the shock is observed at the measuring station until the leading edge reaches the wall.

Figures 6 through 10 show such plots for each Mach number and initial pressure. Each curve corresponds to a different distance from the wall. The times are normalized by $\tau_2$, the mean collision time in the uniform flow behind the incident shock wave. The distances are normalized by $\lambda_2$, the Maxwellian mean free path behind the incoming shock.

$$\tau = \frac{\lambda}{\bar{c}} \qquad (6)$$

$$\lambda = \frac{16}{5}\sqrt{\frac{\gamma}{2\pi}}\,\frac{\mu}{\rho a} \tag{7}$$

$$\bar{c} = \sqrt{\frac{8}{\pi\gamma}}\,a \tag{8}$$

$$\therefore \quad \tau = \frac{4}{5}\,\frac{\mu}{p}$$

$a$ = speed of sound

$\mu$ = viscosity, obtained from reference 12

$\gamma = \frac{c_p}{c_v}$

$c_p$ = specific heat at constant pressure

$c_v$ = specific heat at constant volume

3.2 Density Profiles

Figures 11 through 15 show the plots of density versus distance from the wall at different times for each M and initial pressure. The abscissa is the distance from the wall normalized by $\lambda_2$ given by equation (7). These graphs are obtained by a cross-plot from figures 6 through 10.

The dashed line indicates the limit of the thermal layer, computed according to the boundary-layer theory,

$$\delta = \frac{2}{\sqrt{\pi}} \sqrt{K_5 t} \tag{9}$$

t = time after the shock wave reaches the wall

$$K = \frac{k}{\rho c_p} \tag{10}$$

k = thermal conductivity

The values of the thermal diffusivity $K_5$ are calculated assuming a constant Prandtl number Pr = 2/3 and using the ideal-gas conditions behind the reflected shock.

$$Pr = \frac{\nu}{K} = \frac{2}{3} \tag{11}$$

$$\nu = \frac{\mu}{\rho} \tag{12}$$

$$\therefore \quad K_5 = \frac{3}{2} \frac{\mu_5}{\rho_5} \tag{13}$$

Figures 16 through 20 are obtained from figures 11 through 15 by defining the Lagrangian coordinate $\psi$ which stretches the abscissa proportionally to the local density:

$$\psi = \int_0^X \frac{\rho(X,t)}{\rho_2} \, dX \qquad (14)$$

$$X = \frac{x}{\lambda_2}$$

$x$ = distance from the wall

The significance of this choice of coordinates is discussed in section 4.1. The integration is performed numerically along the lines of constant $t/\tau_2$. The first two points are obtained by the trapezoidal rule, extrapolating linearly to the wall. For the integration from the third point on, a Newton's second-degree polynomial is fitted to the experimental values of density.

3.3 x-t Diagram

Figures 21, 22 and 23 present the experimental x-t diagrams for M = 6, 4 and 3 respectively, obtained from figures 6 through 10. The theoretical thermal layer thickness, defined by equation (9), is also shown, as well as some lines of constant density. The co-slope W of the trajectory of the reflected shock defines the speed $u_R$ of the reflected shock (in laboratory coordinates) normalized by the mean molecular speed $\bar{c}_2$ (Eq. 8) in the uniform flow behind the incident shock. The leading edge of the wave is used for this purpose because its location is determined more accurately and more consistently than that of the trailing edge.

$$M_R' = \frac{u_R + u_2}{a_2} = \sqrt{\frac{8}{\pi\gamma}}\, W + \frac{u_2}{a_2} \qquad (15)$$

$u_2$ = flow velocity in region 2.

## 3.4 Wall-Density History

The three lower curves of figure 24 are wall density histories ($\rho_w \equiv \rho(x = 0+,t)$) for three different initial pressures. Such curves are obtained from figures 16 through 20 by extrapolating the density profiles to $\psi = 0$ for each value of $t/\tau_2$.

It can be seen that the density at the wall is a strong function of the pressure and practically independent of the Mach number, for the times studied, when density and time are normalized as shown. At $p_1 = 15$ μHg there is good agreement between the curves for M = 6 and M = 4, except for large times, when the values of the wall density for M = 4 fall slightly below the curve for M = 6. This difference is at most 3%. At $p_1 = 50$ μHg the curve for M = 3 also falls below that for M = 4 for large times, but in this case the difference is larger (7% for $t/\tau_2 = 140$).

The upper curve will be discussed in section 4.3.

## 3.5 Density Profiles of the Incident Shock Wave

Figures 25 through 27 show the density profiles of the incident shock for Mach = 6, 4 and 3 respectively. Each graph shows the profiles obtained in two different ways: from a single run; and by cross-plotting. The single run method uses the density history from one run and converts the time axis linearly into distances by means of the measured velocity of the shock (see details in Ref. 3). The cross-plot values are taken from the curves for negative $t/\tau_2$ on figures 11 through 15 and plotted in an expanded scale, normalizing the abscissa by $\lambda_1$, the Maxwellian mean free path in the initial gas ahead of the shock. For Mach = 6 and 4 some of Schmidt's results (Ref. 3) are also shown.

It is quite clear that both methods are consistent, although the cross-plot data show a little more scatter, as should be expected, because this method requires more manipulation of the results, introducing more noise in the process. It is also interesting to notice that the uncertainty introduced by the finite width of the oscilloscope trace increases with density.

# IV. DISCUSSION

## 4.1 Density Profiles

Figures 11 through 20 show that, although the incident shock can be clearly distinguished at negative times, the approaching wave disappears into the wall at small positive times! This very interesting fact is evidently due to the development of the thermal layer which acts as a receding wall and whose effects on both incident and reflected shock waves are outlined in chapter I.

The disappearance of the incident wave and the formation of the reflected shock are clearly shown in figures 11 through 20. Of special note is the fact that at some value of $t/\tau_2$ between 3 and 5 the density is almost constant everywhere, i.e., its spacial derivative is almost zero everywhere, although the derivatives with respect to time are of course very large near the wall. Subsequently, the density near the wall continues to increase very rapidly and for a while the entire disturbance in the flow is confined to a small region just a few mean free paths thick. The slope of the density profile is monotonic during the initial stages of the reflection process and no structure suggestive of a shock wave is evident. Finally, at about $t/\tau_2 = 10$ the shock begins to reform and this evidently occurs only as it

emerges from the thermal layer (see Figs. 11 through 15).

At later times the reflected shock front is well defined and the corresponding density jump increases, indicating a strengthening which is presumably due to the pressure waves emitted from the thermal layer ("receding wall"). This strengthening is consistent with the acceleration of the shock front shown in the x-t diagrams (Figs. 21,22 and 23). Between the reflected shock and the thermal layer the slopes of the density profiles are small. The density immediately behind the shock is smaller than that given by ideal-shock conditions because the shock is weaker than in the ideal case. But closer to thermal layer the density is larger, becoming larger even than the ideal value. This density increase toward the wall is thought to be caused both by the compression waves emitted by the thermal layer and by the entropy variation in that region. As pointed out in chapter I, both causes tend to increase the density.

Inside the dense thermal layer the temperature (entropy) is reduced by heat transfer to the wall, creating very steep density gradients. To permit a better analysis of this region the abscissas in figures 16 through 20 are stretched proportional to the local density. From the definition of $\psi$ (Eq. 14) it can be seen that its value is proportional to the mass of gas between the corresponding station and the wall. $\psi$ is also proportional and nearly

equal to the number of local mean free paths between that location and the wall. Therefore, $\psi$ is a more meaningful parameter for exhibiting phenomena dominated by collisional processes.

In this coordinate system the severe slopes in the density profiles near the wall are greatly reduced because higher densities imply smaller mean free paths and, as $\psi$ measures the number of mean free paths, it is stretched proportionately. The curvature of the density profiles near the wall is also reduced, permitting a more reliable extrapolation to estimate the values of the density at the wall (Secs. 3.4 and 4.3).

In non-equilibrium flows of rarefied gases an important parameter that measures the magnitude of the departures from equilibrium is the relative change of a variable per local mean free path. From figures 16 through 20 it is seen that the maximum relative variation of density per local mean free path increases with time until about $t/\tau_2 = 7.5$ and then decreases again. The point of maximum gradient is located about two mean free paths from the wall at $t/\tau_2 = 7.5$, and about six mean free paths at $t/\tau_2 = 80$ or 90. The maximum relative density change varies from 16% to 24% per local mean free path for $t/\tau_2 = 7.5$ and is about 7% for $t/\tau_2 = 80$ or 90. For normal shocks, at the point of maximum slope this value is approximately 13% for $M = 6$.

## 4.2 x-t Diagram

Figures 21 through 23 show the non-dimensional x-t diagrams for M = 6, 4 and 3, respectively. The speed W of the reflected shock increases toward the ideal-shock value as the wave front moves away from the wall. As the normalizing constants for both space and time depend linearly on the pressure, the slopes (velocities) do not contain any pressure-dependent scaling factor. Therefore, as both trailing and leading edges of the incident (Fig. 22) and reflected waves are the same for both pressures plotted in each figure (Figs. 21 and 22), the velocity W must be independent of the pressure, as expected. Also, the shock thickness scales linearly with pressure, as expected.

The lines of constant density indicate a pressure dependence in the inviscid region between the reflected shock and the thermal layer. As explained in chapter I and in section 4.1, the density near the thermal layer is thought to be determined mainly by the entropy gradients, whose effects depend strongly on the development of the thermal layer. For higher initial pressures the displacement velocity is less, so departures from ideal are smaller and the entropy behind the reflected shock is higher. Higher entropy corresponds to lower density. Therefore, the lower normalized densities observed in the runs with higher initial pressures are consistent with the above explanation.

## 4.3 Wall Density History

Boundary-layer theory (no slip) predicts that the asymptotic values of the normalized wall densities are 30.9, 14.2 and 8.15 for M = 6.00, 4.00 and 2.96, respectively. These theoretical asymptotic values are of course independent of the initial pressure. The present results, shown on figure 24, fall much below the predicted values, indicating that accommodation (slip) effects are large, and are indeed a function of the initial pressure. For example, the smallest value of $T_w \equiv T(0+,t)$, the temperature of the gas at the wall, implied by figure 24 corresponds to $(\rho_w - \rho_1)/(\rho_5 - \rho_1) = 5$ at M = 4 and $p_1$ = 15 μHg, that is, $T_w = 835^{\circ}K$, in contrast with the value $300^{\circ}K$ which would be found if there were no thermal slip. For M = 6 and $p_1$ = 35 μHg, $(\rho_w - \rho_1)/(\rho_5 - \rho_1) = 3.17$ (Fig. 24) gives $T_w = 2850^{\circ}K$!

In the above figure 24 the normalizing constant $\tau_2$ is inversely proportional to the initial pressure. If, however, the normalized time is divided by the square root of the initial pressure, the values of the abscissa become proportional to the square root of pressure. For convenience of plotting this is done by multiplying the values of the density by the square root of initial pressure, which has an equivalent effect. In doing this, it is found that the results for all Mach numbers and initial pressures collapse onto a single curve shown at the top of figure 24,

indicating that the proper scaling factor for the wall density is the square root of the pressure. Therefore, it appears that near the wall the time should be normalized by an "accommodation time" which is inversely proportional to the square root of the pressure. In a completely different experiment, Busing and Clarke (Ref. 13) also concluded that accommodation effects at the wall scale with the square root of the pressure.

It should be pointed out, however, that the uncertainties of this plot are higher than the values given in section 2.4 for the other results, because figure 24 is obtained by extrapolation. An error of 3% in the values of the density and 5% in the distance in figures 16 through 20 may cause a deviation of as much as 25% in the values of the wall density. However, the scatter in figure 24 suggests that 25% would be too pessimistic and that the accuracy of such plot seems to be better than that.

# V. CONCLUSIONS

1) The choice of density as the principal variable turns out to be very fruitful because it carries information about the variation of other parameters such as temperature, pressure and entropy, as they are influenced, for example, by heat transfer or shock strength.

2) The plots of density profiles have sufficient resolution and accuracy that both quantitative and qualitative information can be obtained about a) the interaction of the incident shock wave with the wall, b) the effects of the wall heat transfer and accommodation on the density near the wall, c) the formation of the reflected shock wave, its strength and trajectory on the x-t diagram, and d) the nature of the flow field lying between the thermal layer and the reflected shock wave at "large times" (large for this experiment).

3) By stretching the normalized distances proportionally to the local mean free path, the very steep slopes in the density profiles near the wall are greatly reduced, permitting a more reliable extrapolation of the density profiles to the wall. The wall-density histories so obtained indicate very large accommodation effect.

## REFERENCES


1. M. Camac, "Rarefied Gasdynamics", Vol. 1, p. 240 (Academic Press, Inc., New York, 1965).

2. David A. Russell, "Rarefied Gasdynamics", Vol. 1, p. 265 (Academic Press, Inc., New York, 1965).

3. Bernd J. F. Schmidt, to be published.

4. H. M. Mott-Smith, Phys. Rev., Vol. 82, p. 885 (1951).

5. H. W. Liepmann, R. Narasimha and M. T. Chahine, Phys. Fluids, Vol. 5, p. 1313 (1962).

6. G. A. Bird, J. Fluid Mech., Vol. 30, p. 479 (1967).

7. H. W. Liepmann, A. Roshko, D. Coles, B. Sturtevant, Rev. Sci. Instr., Vol. 33, p. 625 (1962).

8. Charles Chang-Ping Wang, Ph.D. Thesis, California Institute of Technology (1967).

9. H. W. Liepmann, A. Roshko, Elements of Gasdynamics, Wiley, New York (1957).

10. Jerome A. Smith, Ph.D. Thesis, California Institute of Technology (1967).

11. Robert M. Bowman, Ph.D. Thesis, California Institute of Technology (1966).

12. I. Amdur, E. A. Mason, Phys. Fluids, Vol. 1, p. 370 (1958).

REFERENCES (cont.)

13. J. R. Busing and J. F. Clarke, Recent Advances in Aerothermochemistry, (Ed. I. Glassman) Vol. 1, p. 165, AGARD Conference Proceedings No. 12 (1967).

14. H. Mirels and W. H. Braun, Non-Uniformities in Shock Tube Flow Due to Unsteady Boundary Layer Action, NACA TN 4021 (1957).

| MACH | $p_1$ μHg | $p_5$ μHg | $T_1$ °K | $T_5$ °K | $\frac{\rho_5}{\rho_1}$ | $\lambda_2$ mm | $\tau_2$ μsec |
|---|---|---|---|---|---|---|---|
| 6.00 | 15 | 3683 | 298 | 8197 | 8.926 | 1.734 | 1.257 |
| 6.00 | 35 | 8593 | 296 | 8141 | 8.926 | 0.737 | 0.534 |
| 4.00 | 50 | 4885 | 296 | 3697 | 7.822 | 0.463 | 0.483 |
| 4.00 | 15 | 1466 | 296 | 3697 | 7.822 | 1.550 | 1.613 |
| 2.96 | 50 | 2301 | 295 | 2078 | 6.530 | 0.470 | 0.628 |

Table 1 - Average Values

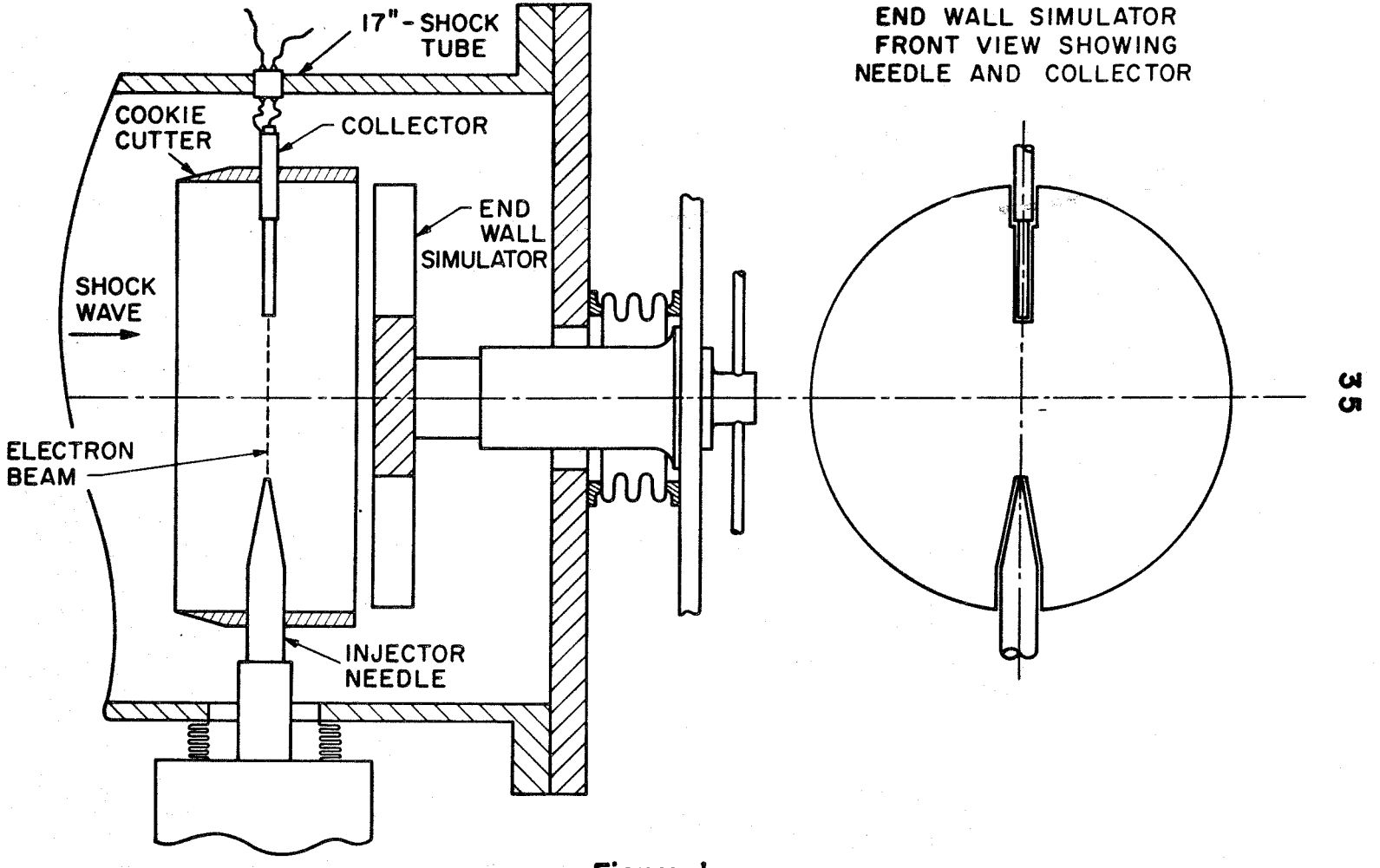
17" - SHOCK TUBE
COOKIE CUTTER
COLLECTOR
END WALL SIMULATOR
SHOCK WAVE
ELECTRON BEAM
INJECTOR NEEDLE
END WALL SIMULATOR
FRONT VIEW SHOWING
NEEDLE AND COLLECTOR

Figure 1

RUN 2016

MACH = 4.01 P1 = 15 μ Hg DIST = 12 m m

Scope # 2

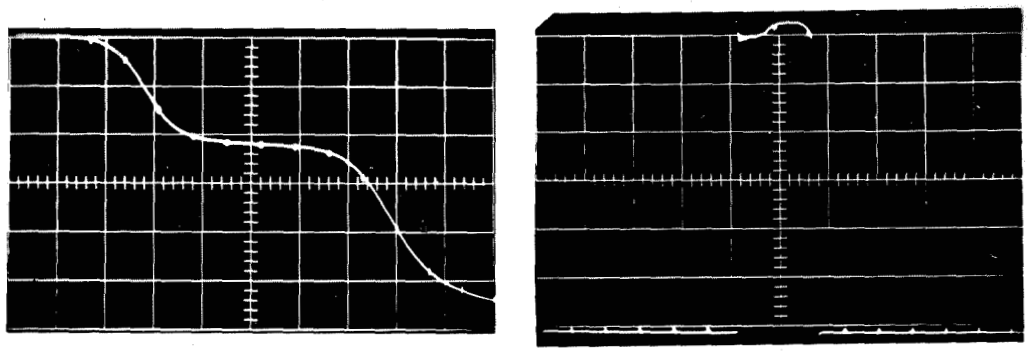

Time marks = 5 μ sec apart

Calibration mark = .85 V

Scope # 3

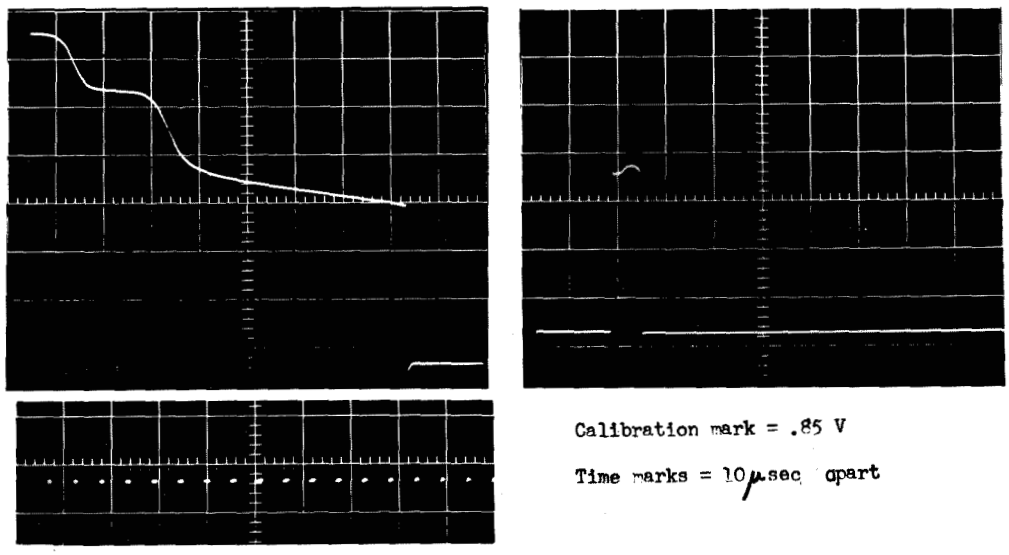

Calibration mark = .85 V

Time marks = 10 μ sec apart

Figure 2

RUN 2913

MACH = 3.97 P1 = 15 $\mu$Hg DIST = 4 m m

Scope # 2

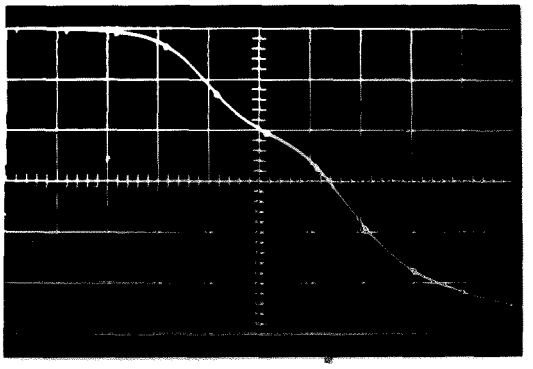

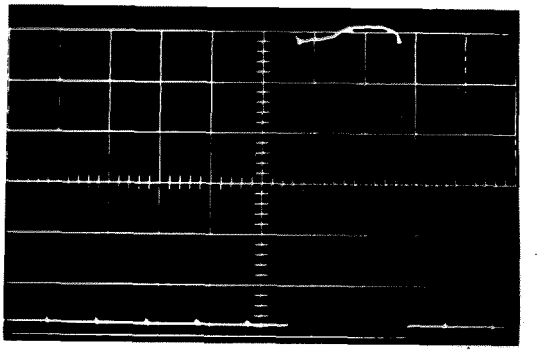

Time marks = 5 $\mu$sec apart

Calibration mark = .85 V

Scope # 3

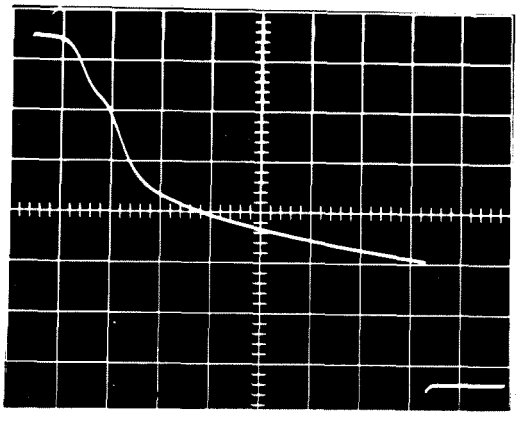

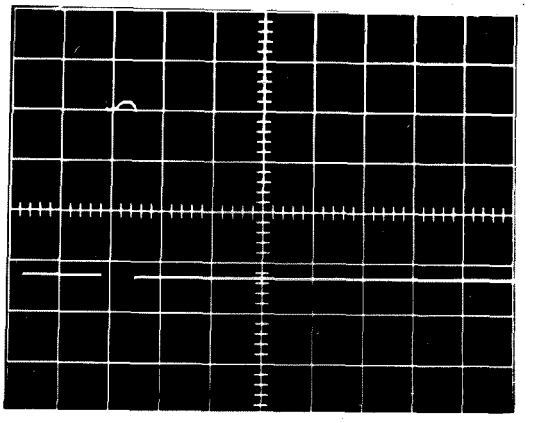

Calibration mark = .85 V

Figure 3

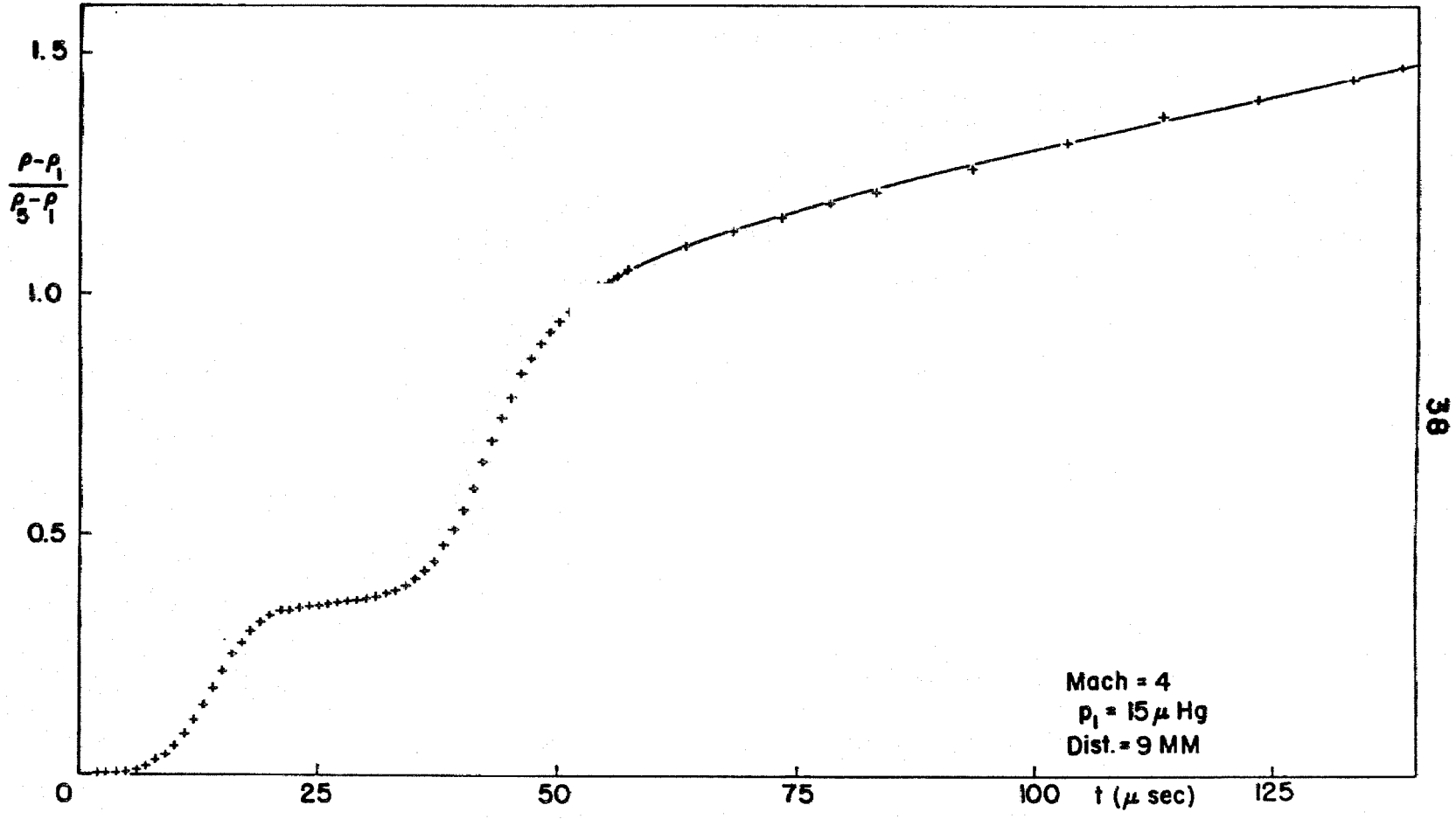


DENSITY VS. TIME

Figure 4

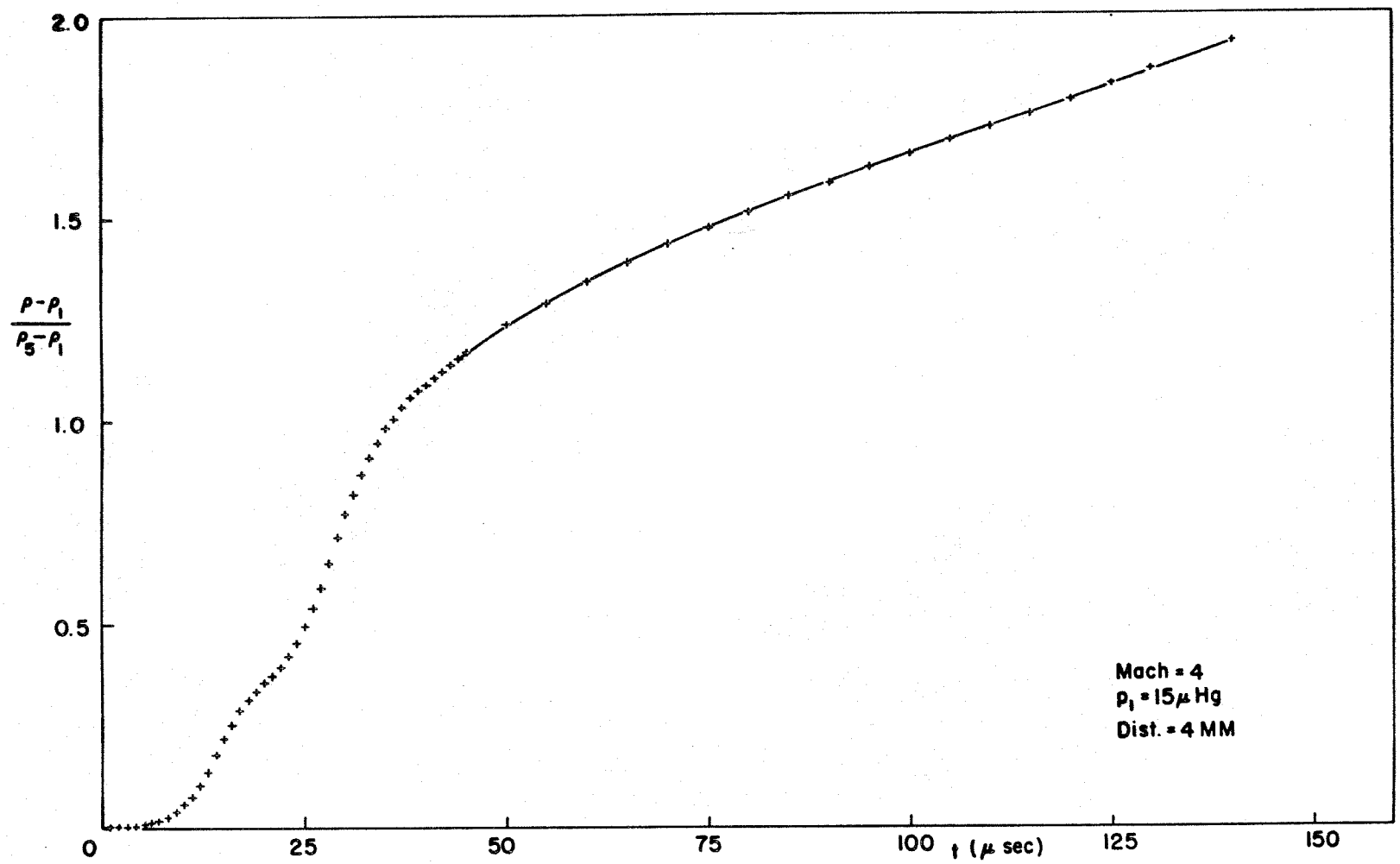


DENSITY VS. TIME

Figure 5

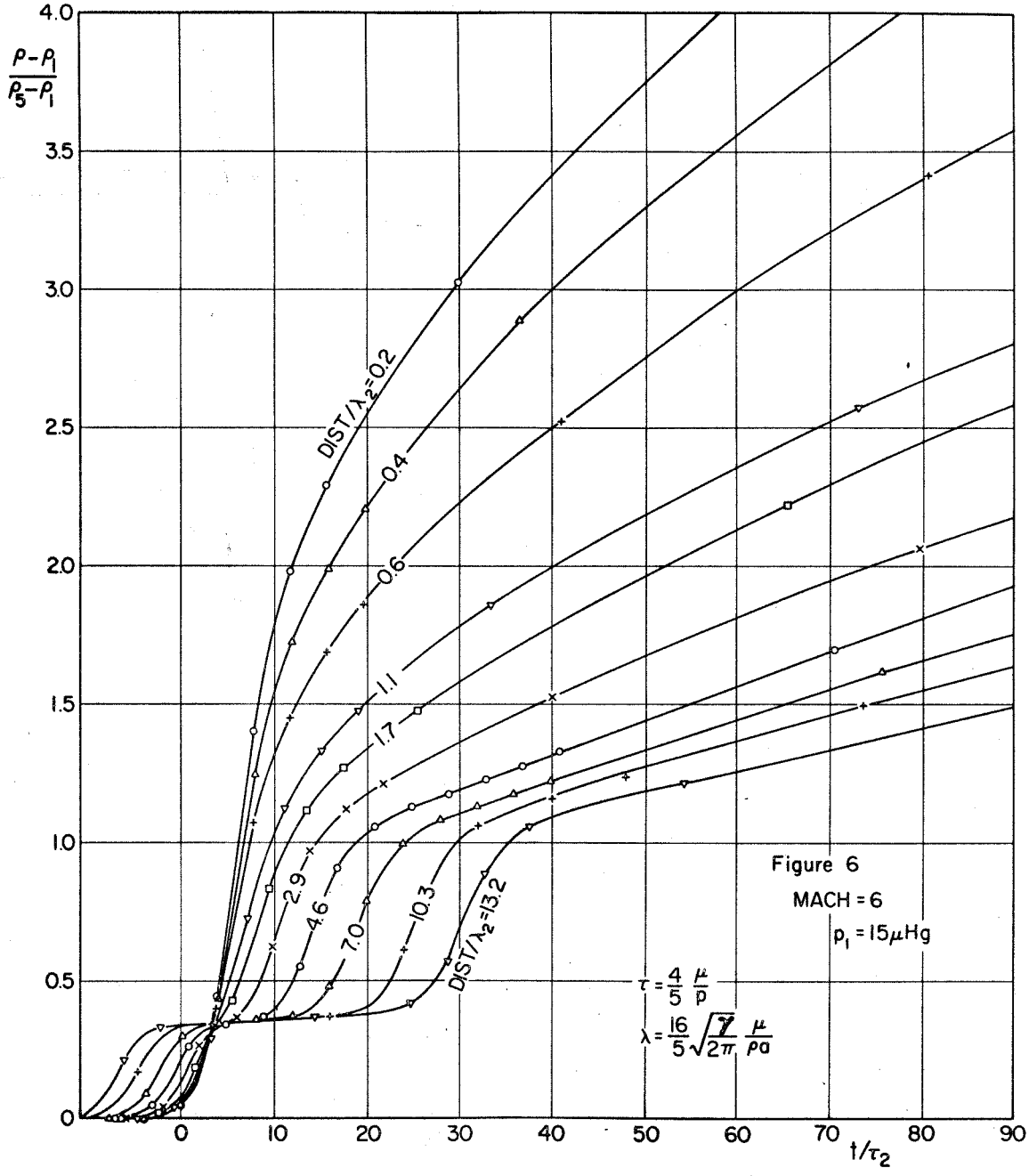
4.0
3.5
3.0
2.5
2.0
1.5
1.0
0.5
0
$\frac{\rho-\rho_1}{\rho_5-\rho_1}$
DIST/$\lambda_2$=0.2
0.4
0.6
1.1
1.7
2.9
4.6
7.0
10.3
DIST/$\lambda_2$=13.2
0
10
20
30
40
50
60
70
80
90
$t/\tau_2$
Figure 6
MACH = 6
$p_1$ = 15μHg
$\tau = \frac{4}{5}\frac{\mu}{p}$
$\lambda = \frac{16}{5}\sqrt{\frac{\gamma}{2\pi}}\frac{\mu}{\rho a}$

FIG. 6

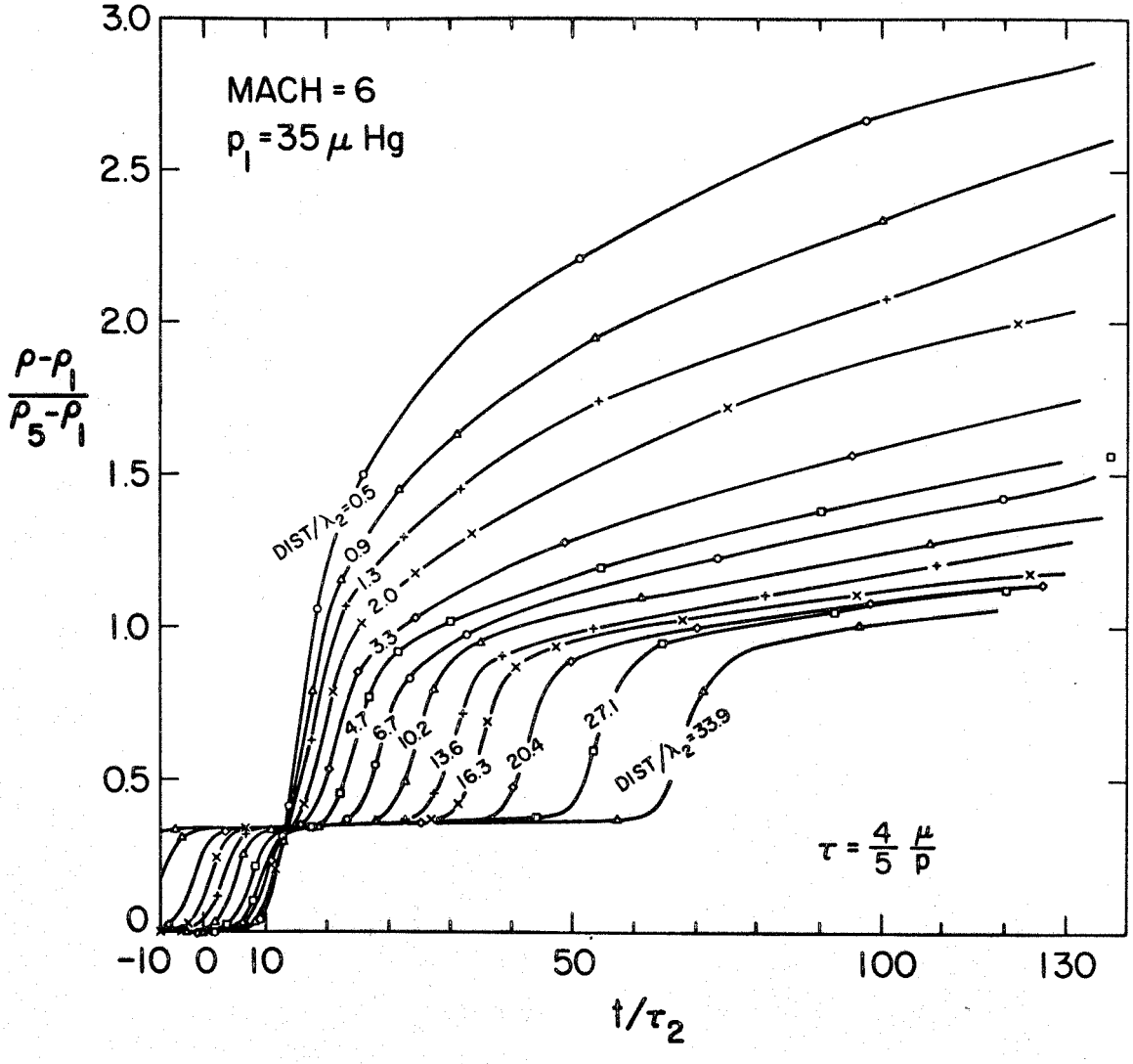
MACH = 6
$p_1 = 35\ \mu$ Hg
$\frac{\rho-\rho_1}{\rho_5-\rho_1}$
DIST/$\lambda_2$=0.5
0.9
1.3
2.0
3.3
4.7
6.7
10.2
13.6
16.3
20.4
27.1
DIST/$\lambda_2$=33.9
$\tau = \frac{4}{5}\frac{\mu}{p}$
$t/\tau_2$
3.0
2.5
2.0
1.5
1.0
0.5
0
-10
0
10
50
100
130

Figure 7

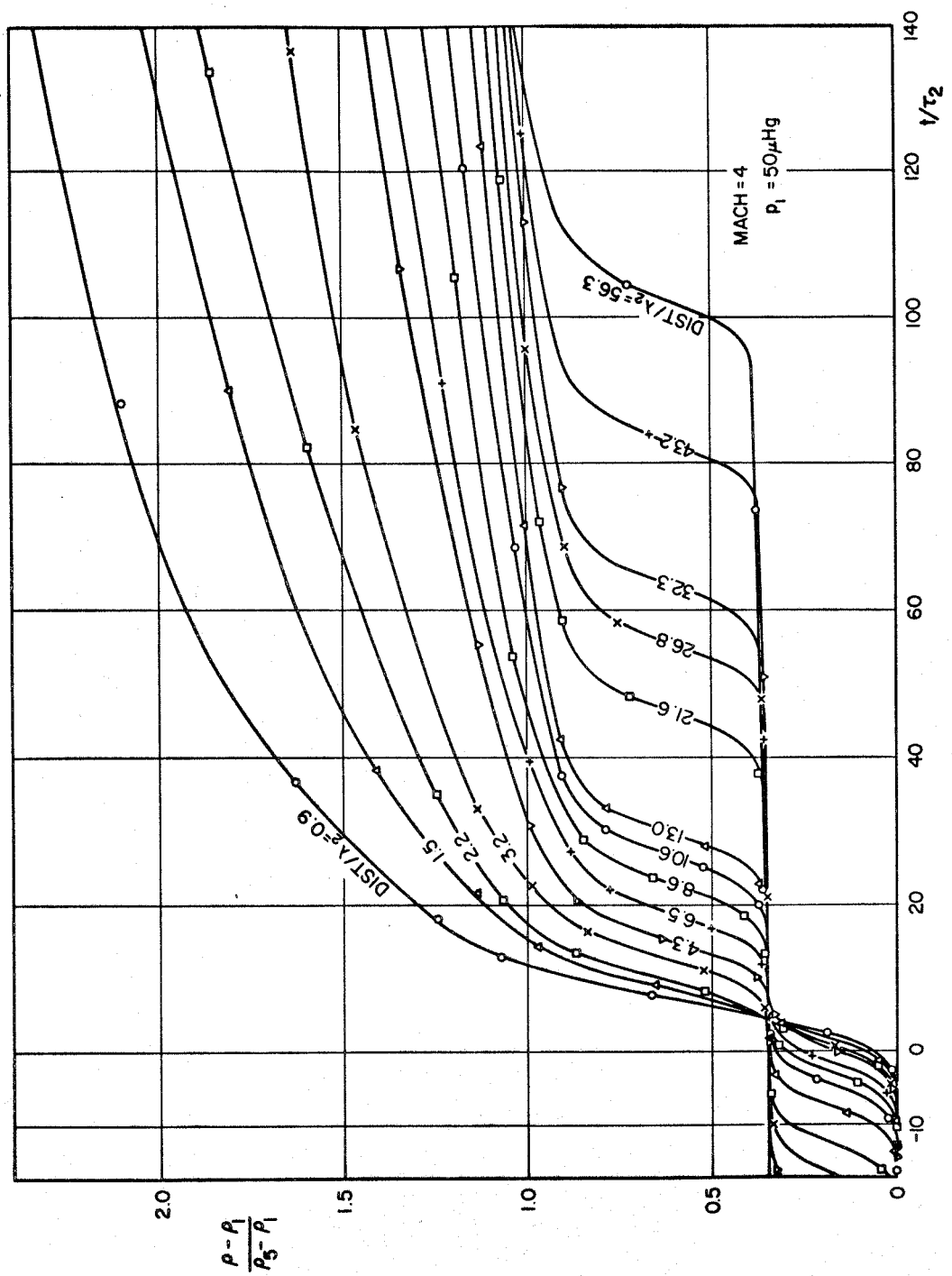
MACH = 4
$p_1 = 50\mu Hg$
DIST/λ2=0.9
1.5
2.2
3.2
4.3
6.5
8.6
10.6
13.0
21.6
26.8
32.3
43.2
DIST/λ2=56.3
$\frac{p-p_1}{p_5-p_1}$
$1/\tau_2$
0
0.5
1.0
1.5
2.0
-10
0
20
40
60
80
100
120
140

Figure 8

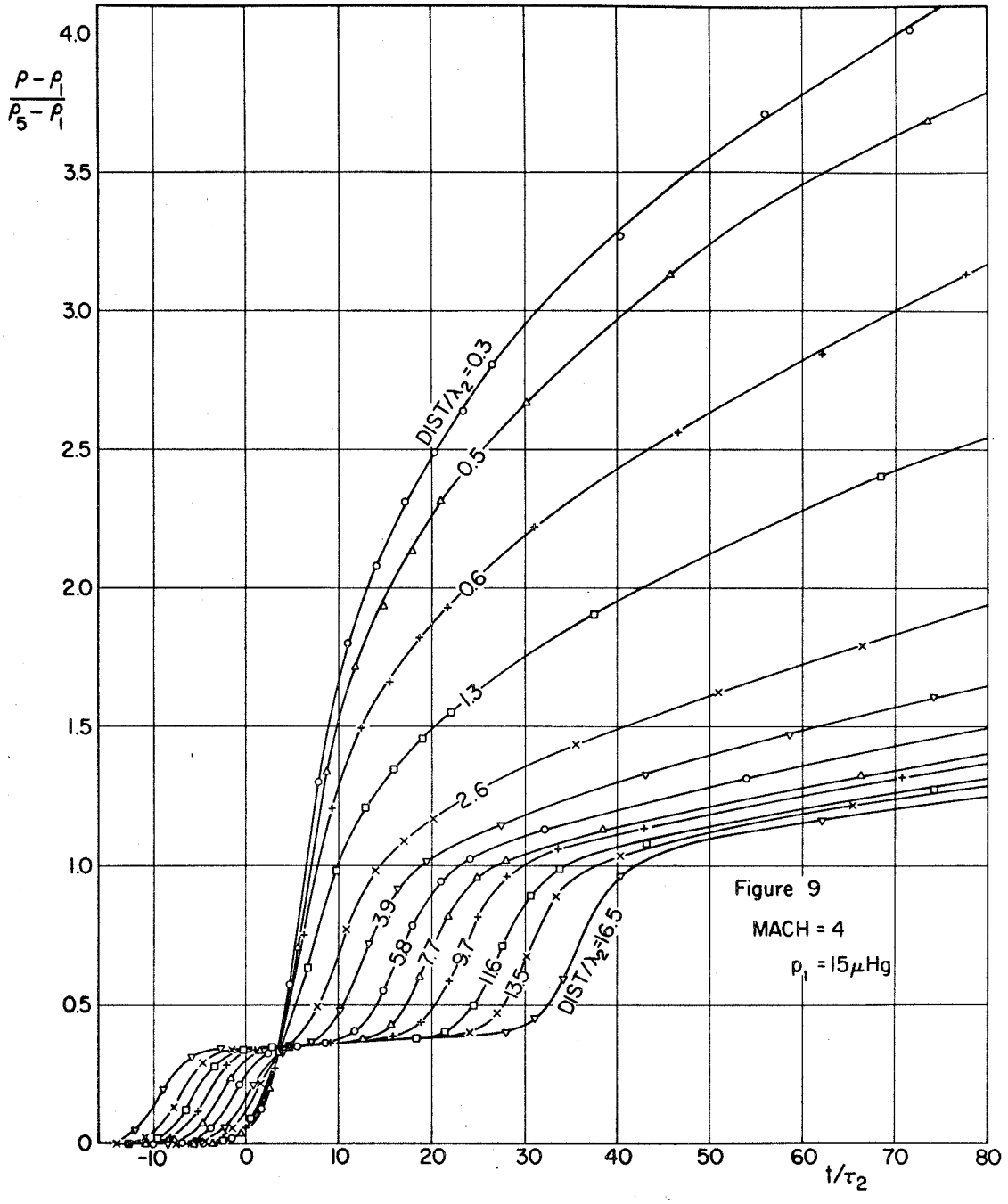
$\frac{\rho - \rho_1}{\rho_5 - \rho_1}$
4.0
3.5
3.0
2.5
2.0
1.5
1.0
0.5
0
-10
0
10
20
30
40
50
60
70
80
$t/\tau_2$
DIST/$\lambda_2$=0.3
0.5
0.6
1.3
2.6
3.9
5.8
7.7
9.7
11.6
13.5
DIST/$\lambda_2$=16.5
Figure 9
MACH = 4
$p_1$ = 15$\mu$Hg

FIG. 9

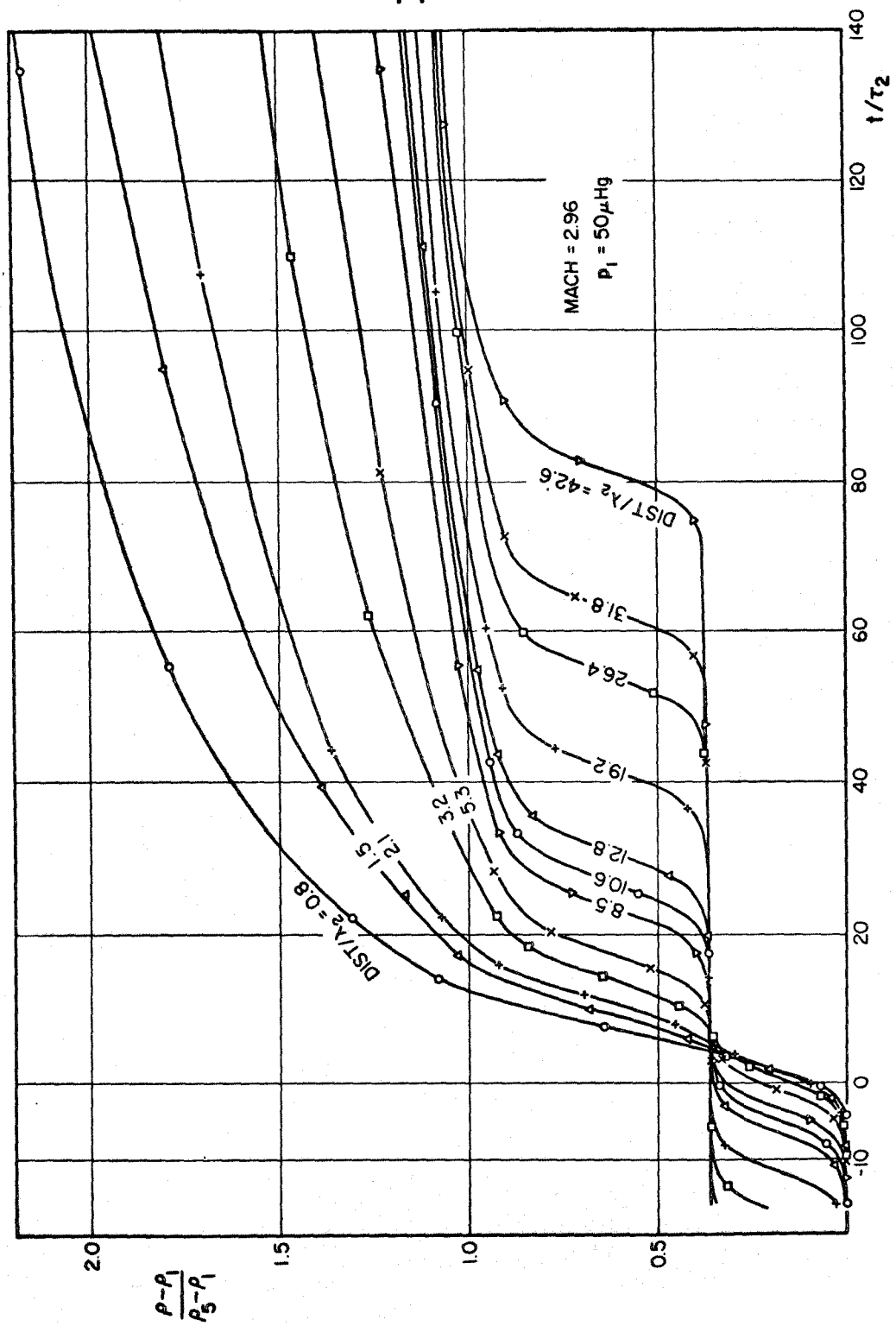
MACH = 2.96
$P_1$ = 50μHg
DIST/λ2 = 0.8
1.5
2.1
3.2
3.5
5.3
8.5
10.6
12.8
19.2
26.4
31.8
DIST/λ2 = 42.6
$\frac{\rho-\rho_1}{\rho_5-\rho_1}$
t/τ2
2.0
1.5
1.0
0.5
-10
0
20
40
60
80
100
120
140

Figure 10

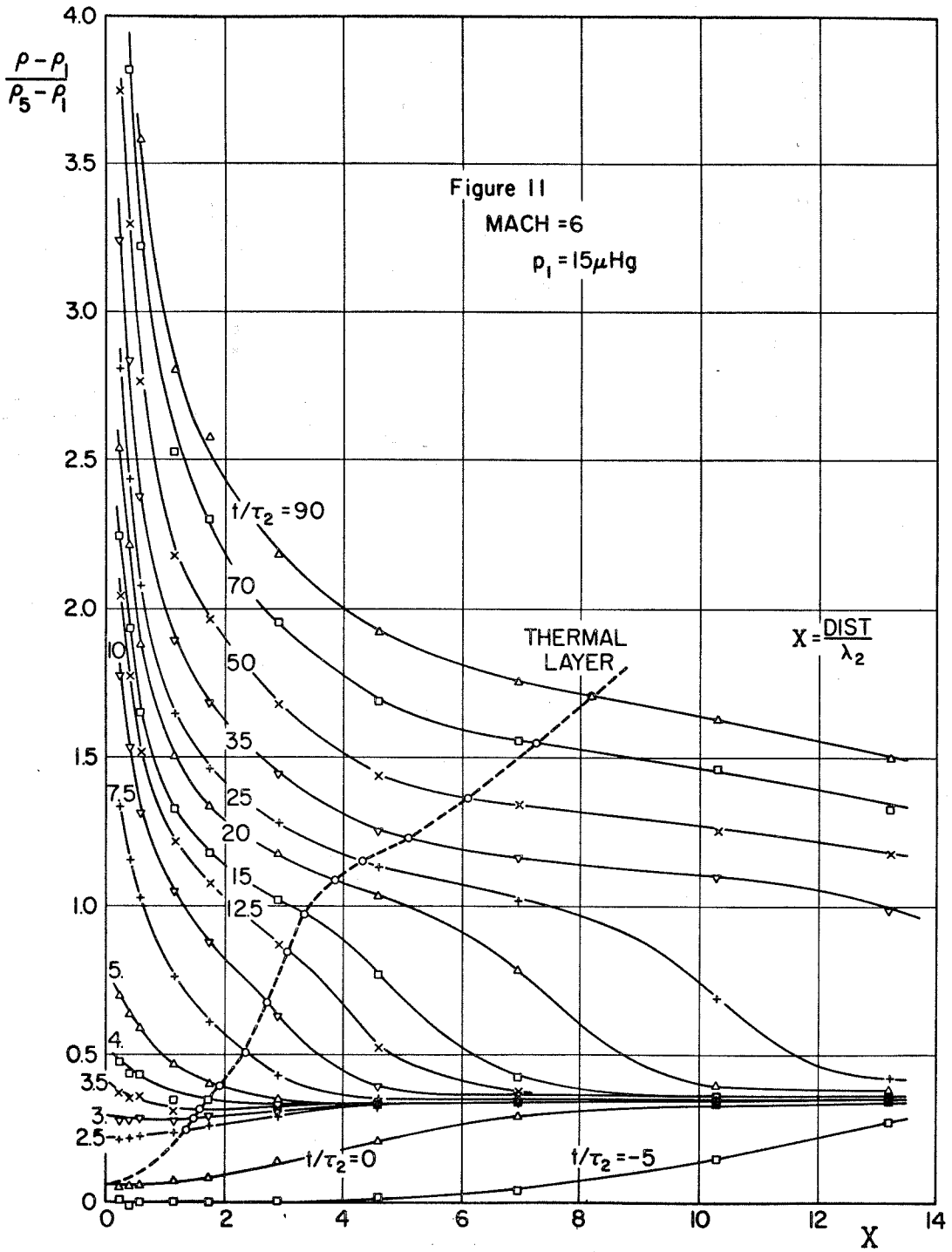
Figure 11
MACH =6
$p_1 = 15\mu Hg$
$\frac{\rho - \rho_1}{\rho_5 - \rho_1}$
$X = \frac{DIST}{\lambda_2}$
THERMAL LAYER
$t/\tau_2 = 90$
70
50
35
25
20
15
12.5
10
7.5
5.
4.
3.5
3.
2.5
$t/\tau_2 = 0$
$t/\tau_2 = -5$
X
0
0.5
1.0
1.5
2.0
2.5
3.0
3.5
4.0
2
4
6
8
10
12
14

FIG. 11

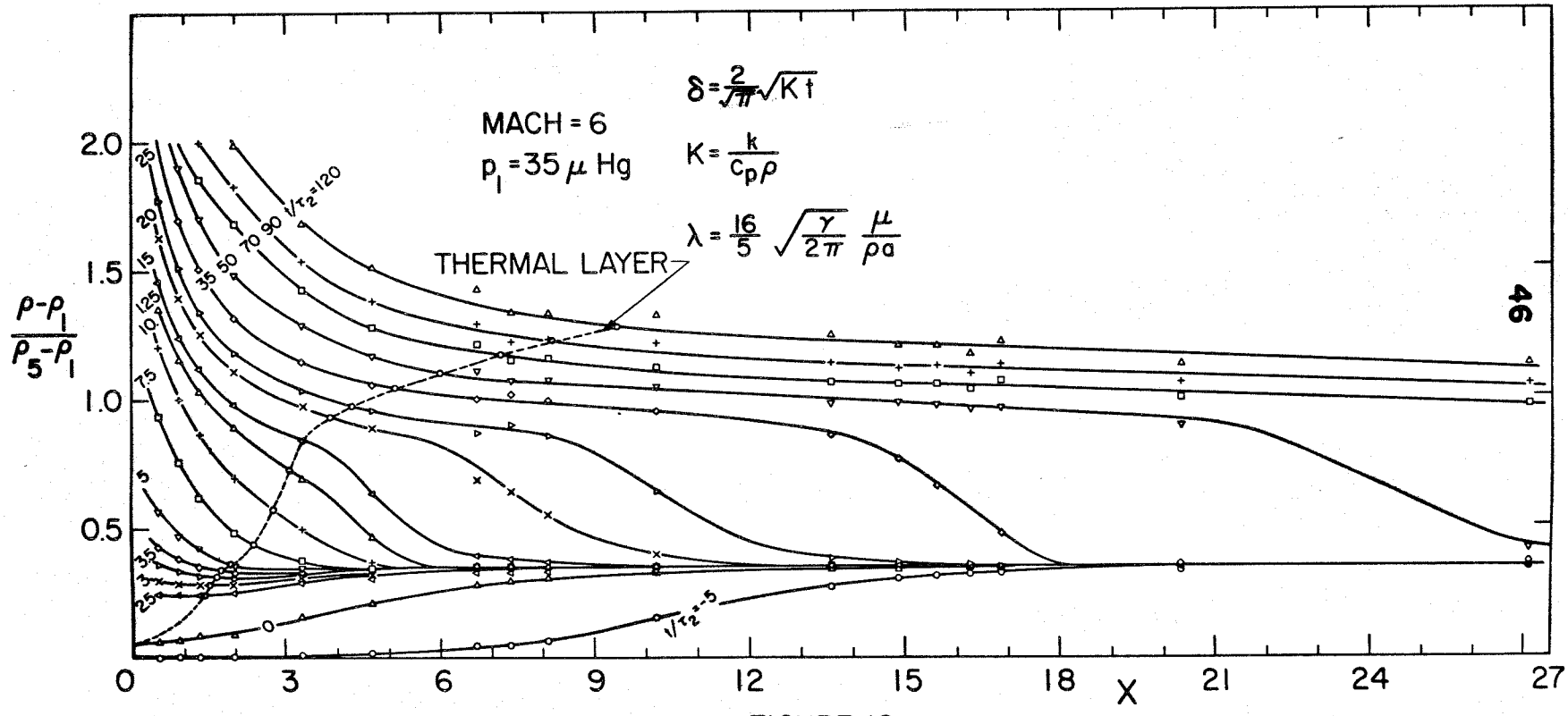
MACH = 6
$p_1 = 35\ \mu$ Hg
$\delta = \frac{2}{\sqrt{\pi}}\sqrt{Kt}$
$K = \frac{k}{c_p \rho}$
$\lambda = \frac{16}{5}\sqrt{\frac{\gamma}{2\pi}}\frac{\mu}{\rho a}$
THERMAL LAYER
$\frac{\rho - \rho_1}{\rho_5 - \rho_1}$
X
$1/\tau_2 = 120$
$1/\tau_2 = 5$
46

FIGURE 12

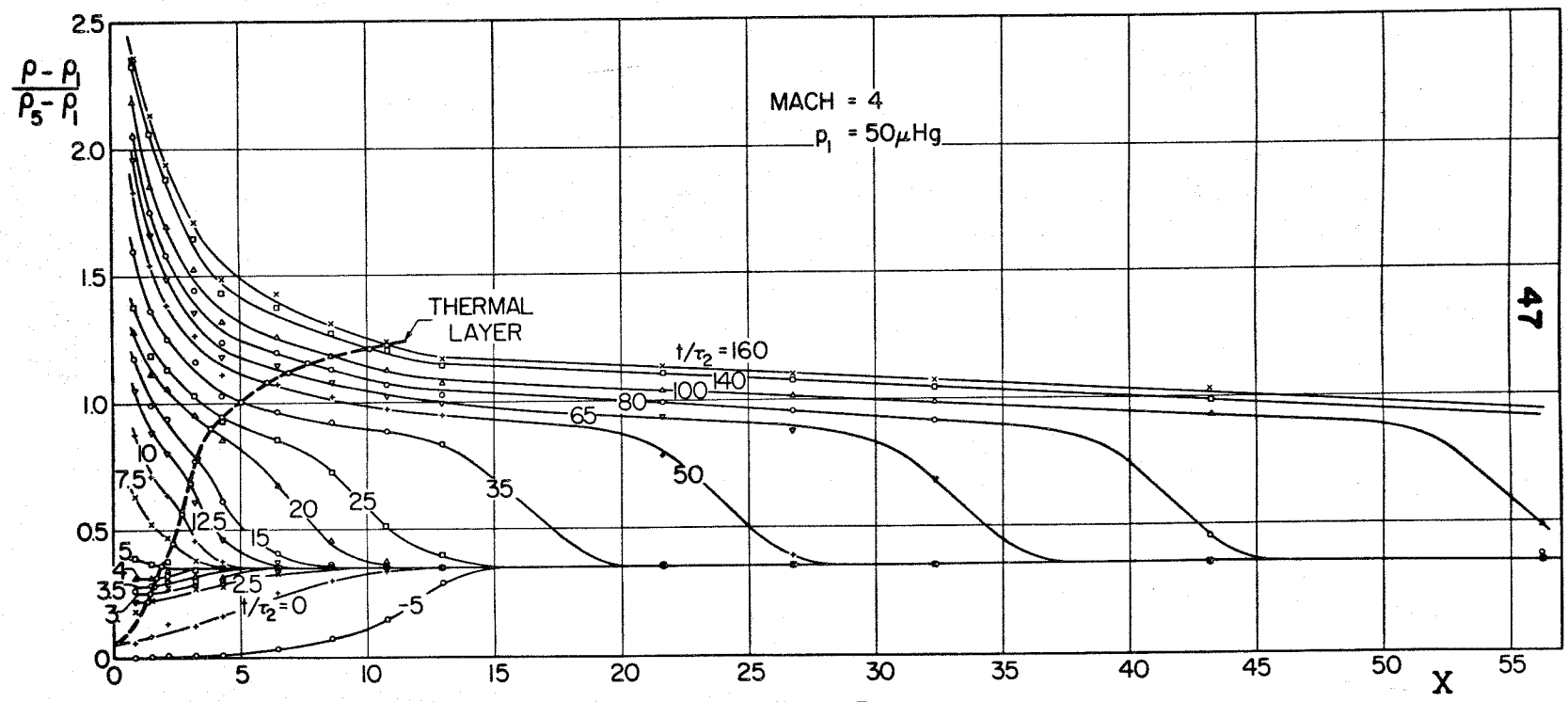
$\frac{\rho - \rho_1}{\rho_5 - \rho_1}$
MACH = 4
$p_1$ = 50μHg
THERMAL LAYER
$t/\tau_2$ = 160
140
100
80
65
50
35
25
20
15
12.5
10
7.5
5
4
3.5
3
2.5
$t/\tau_2$ = 0
-5
X
47

Figure 13

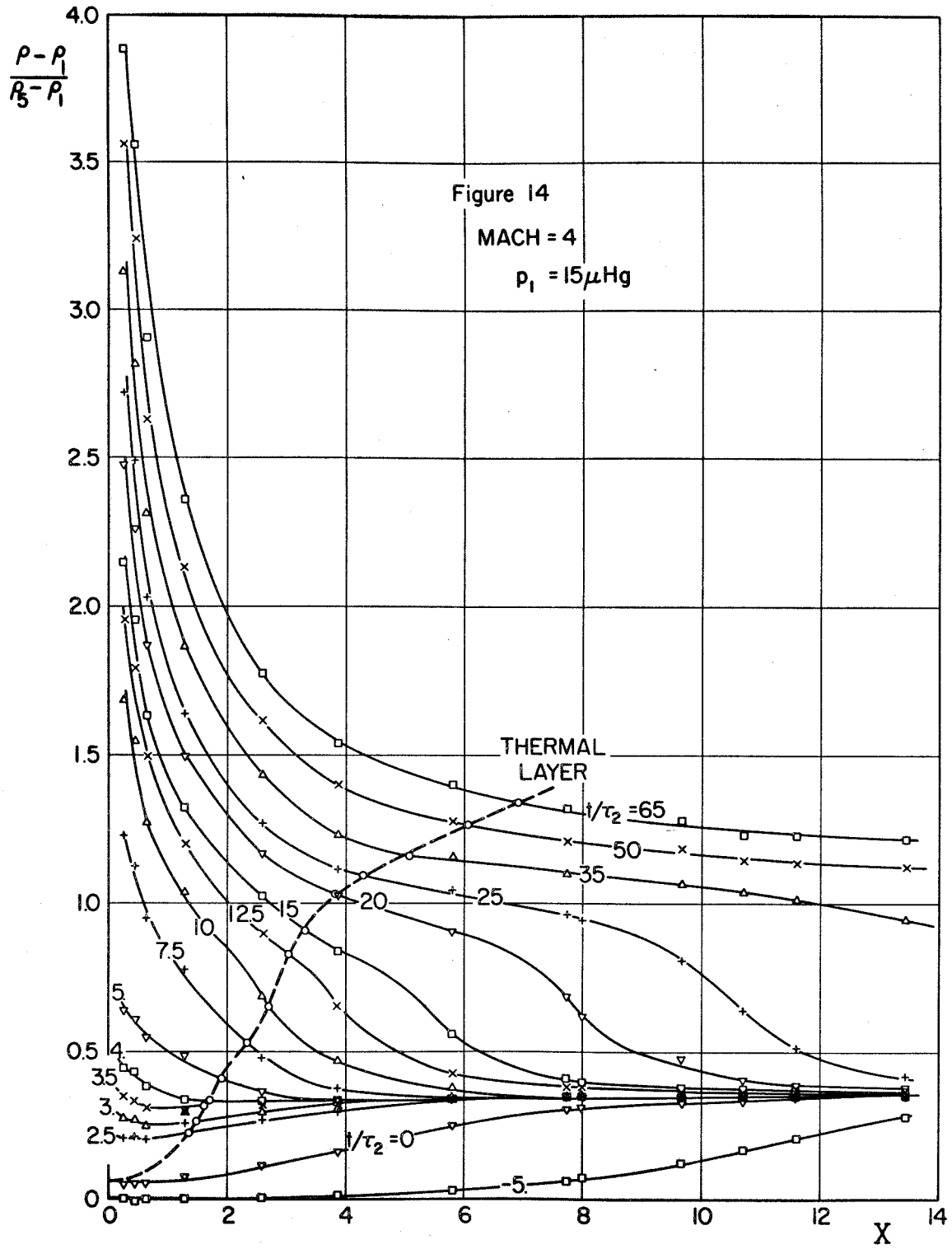
$\frac{\rho - \rho_1}{\rho_5 - \rho_1}$
Figure 14
MACH = 4
$p_1$ = 15μHg
THERMAL LAYER
$t/\tau_2$ =65
50
35
25
20
15
12.5
10
7.5
5
4
3.5
3
2.5
$t/\tau_2$ =0
-5
X

FIG. 14

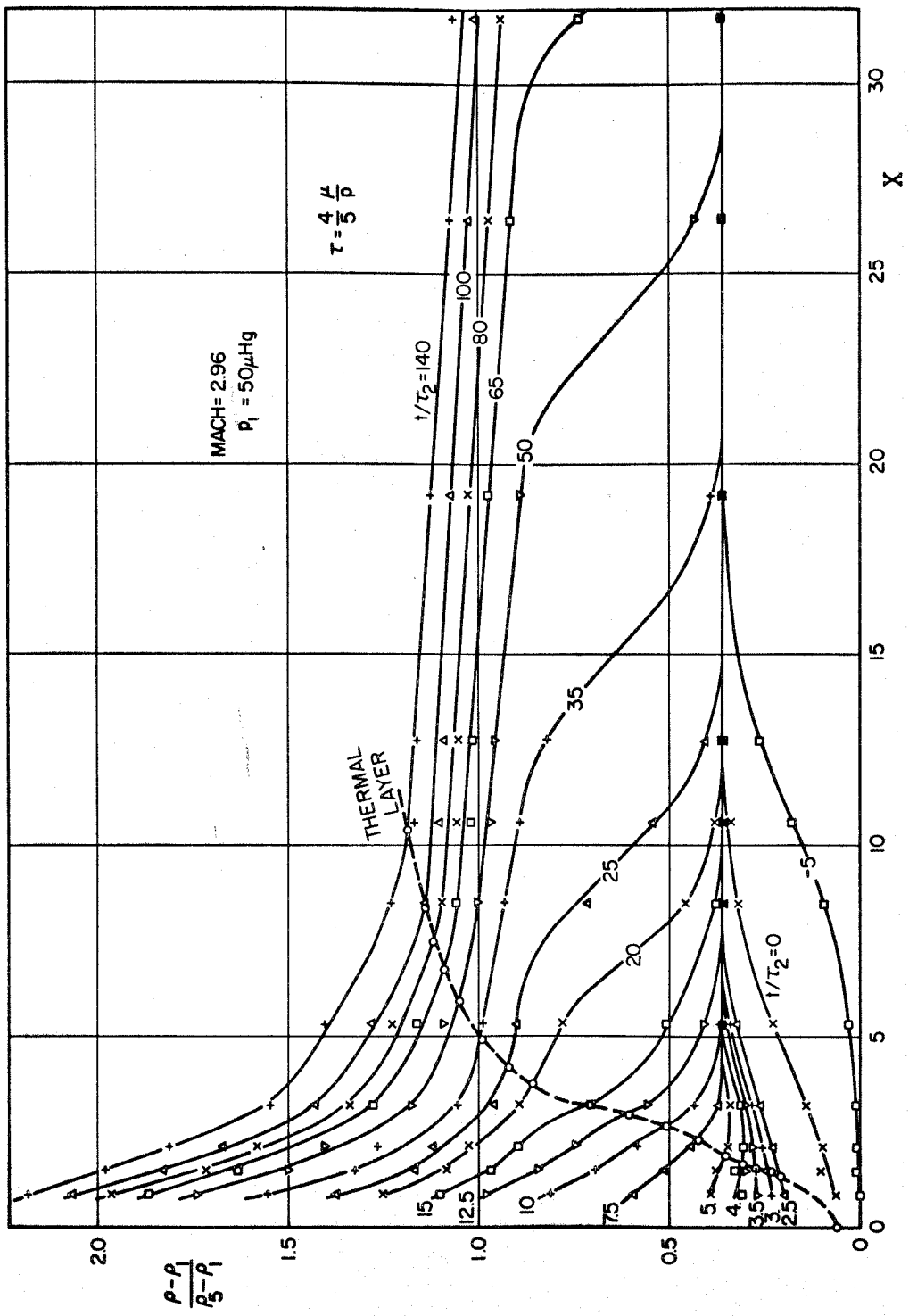
MACH= 2.96
$P_1$ = 50μHg
$\tau = \frac{4}{5}\frac{\mu}{p}$
$1/\tau_2$=140
100
80
65
50
35
25
20
15
12.5
10
7.5
5
4
3.5
3
2.5
$1/\tau_2$=0
-5
THERMAL LAYER
$\frac{p-p_1}{p_s-p_1}$
X
0
5
10
15
20
25
30
0.5
1.0
1.5
2.0

Figure 15

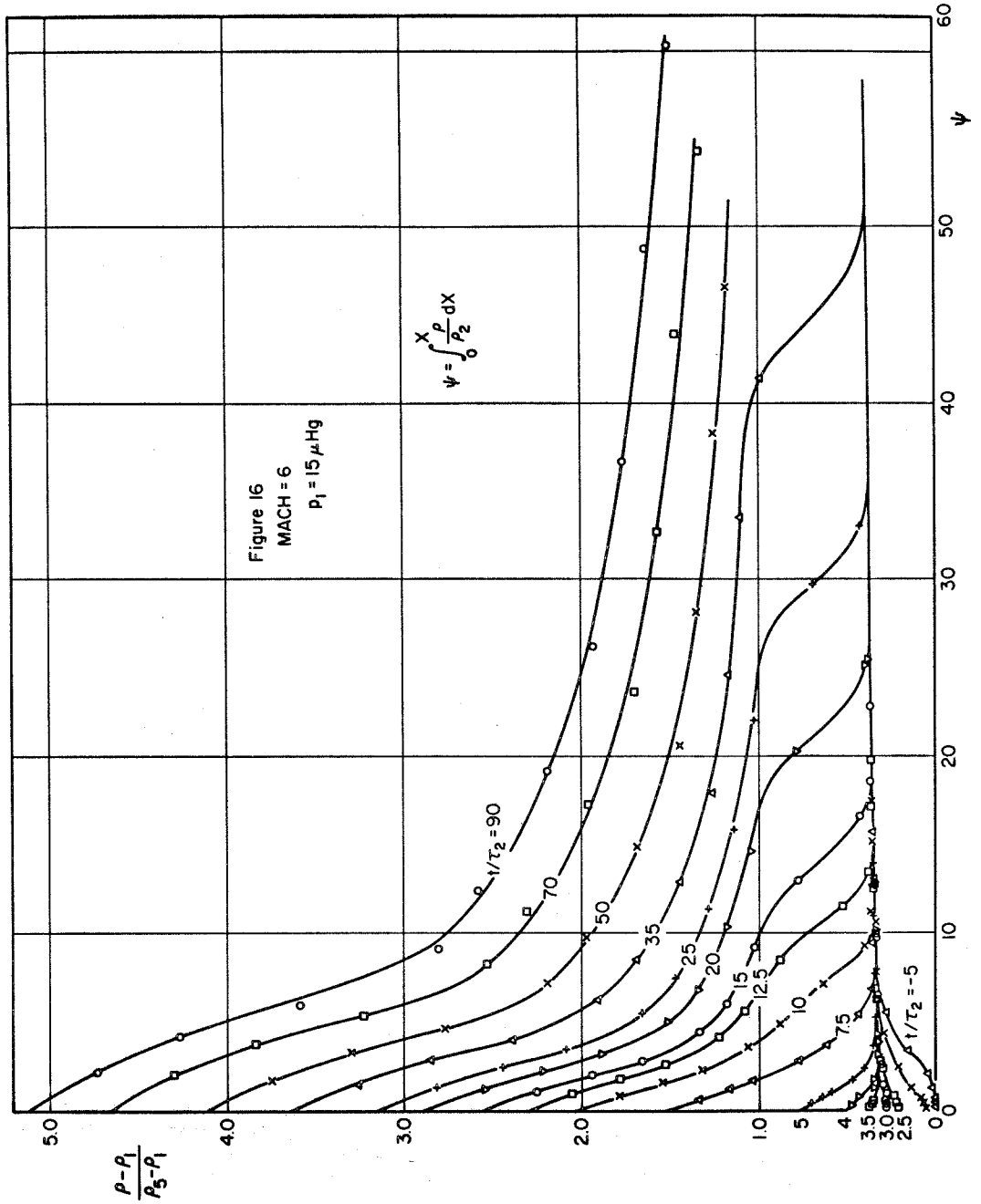
Figure 16
MACH = 6
$p_1$ = 15 μHg
$\psi = \int_0^X \frac{\rho}{\rho_2} dX$
$\frac{\rho - \rho_1}{\rho_5 - \rho_1}$
$\psi$
$t/\tau_2$ = 90
70
50
35
25
20
15
12.5
10
7.5
5
4
3.5
3.0
2.5
$t/\tau_2$ = -5
0
10
20
30
40
50
60
1.0
2.0
3.0
4.0
5.0

FIG. 16

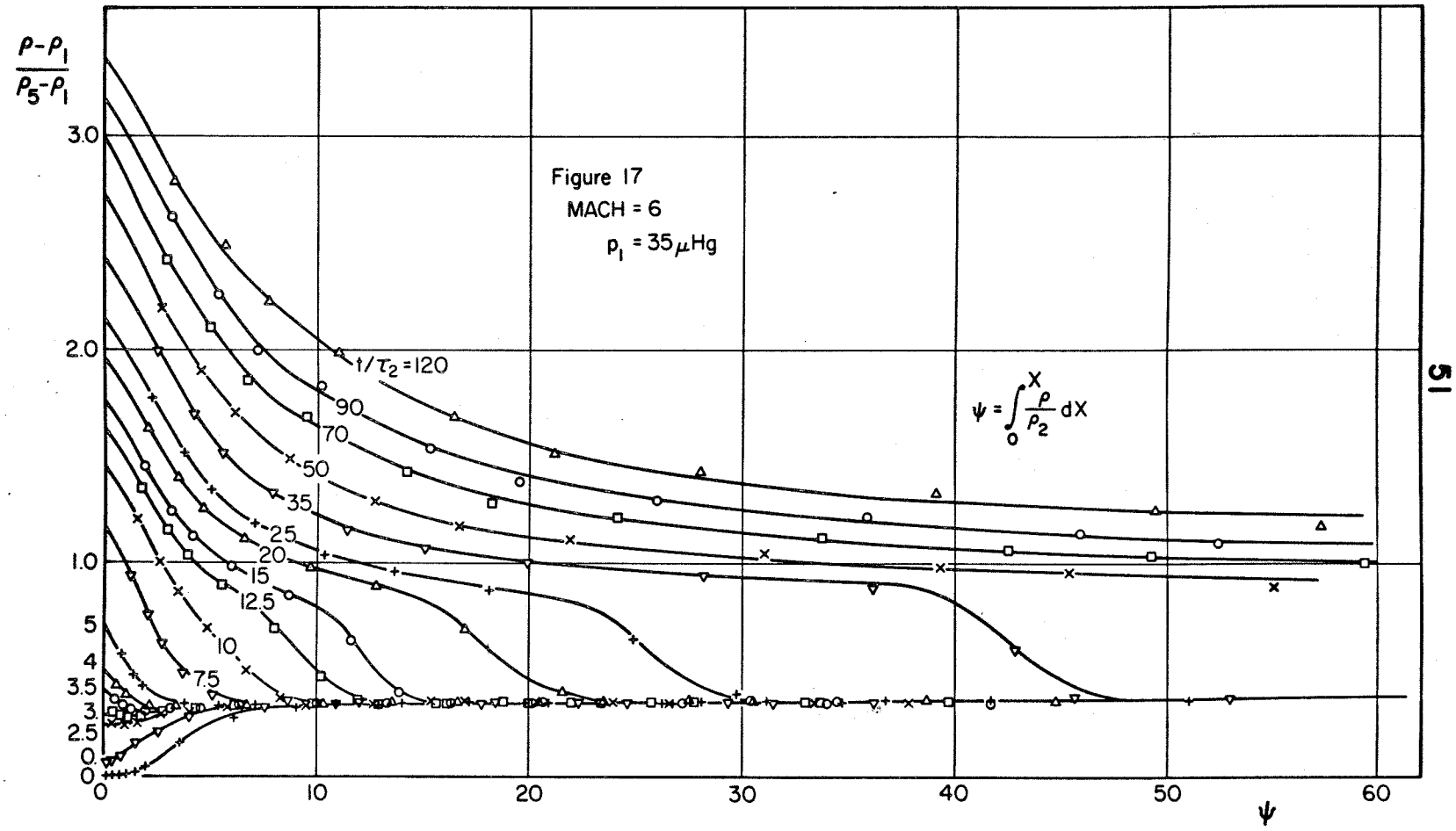
$\frac{\rho-\rho_1}{\rho_5-\rho_1}$
Figure 17
MACH = 6
$p_1 = 35\mu Hg$
$t/\tau_2 = 120$
90
70
50
35
25
20
15
12.5
10
7.5
$\psi = \int_0^X \frac{\rho}{\rho_2} dX$
3.0
2.0
1.0
5
4
3.5
3
2.5
0
0
0
10
20
30
40
50
60
$\psi$

FIG. 17

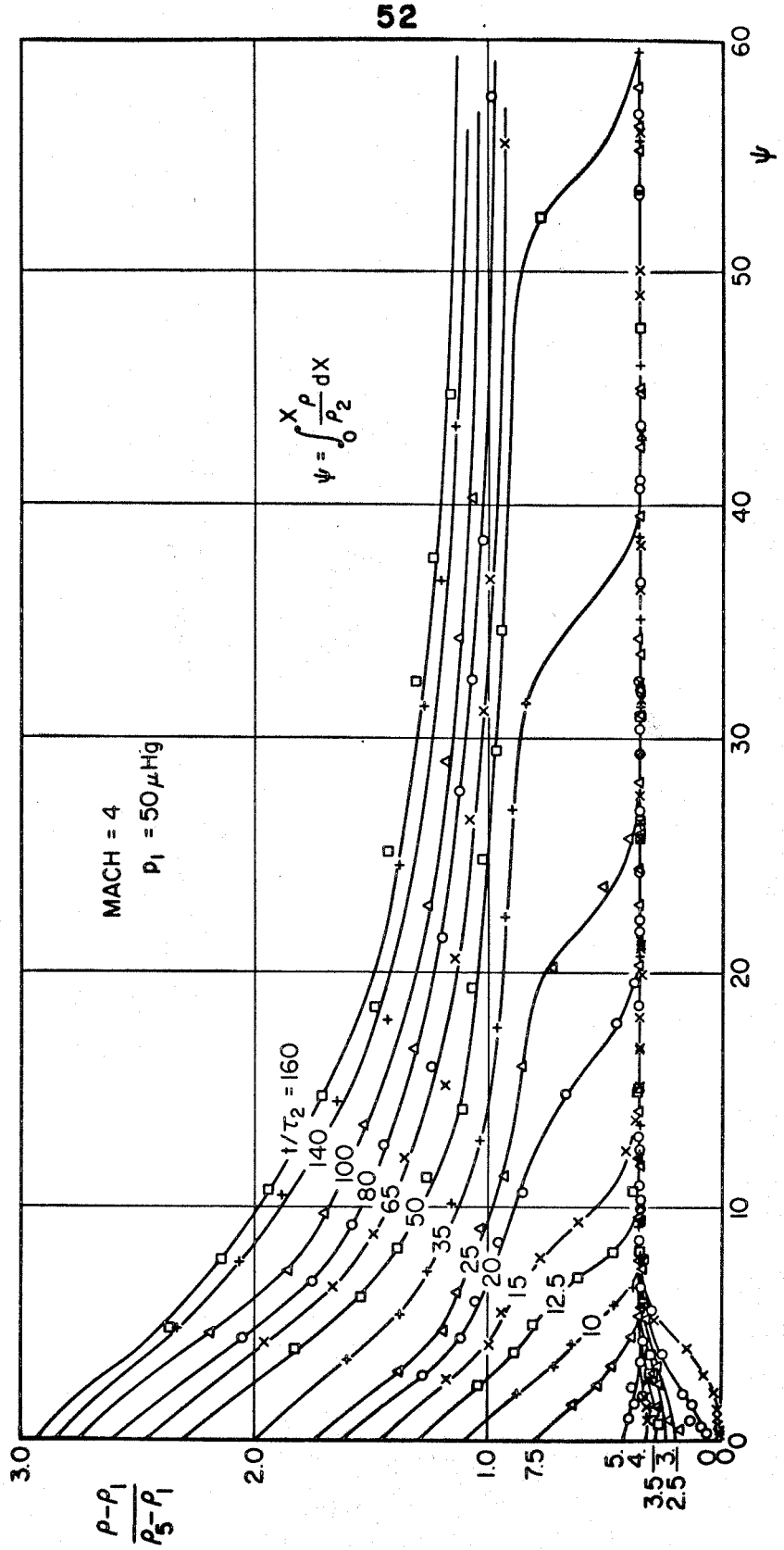
MACH = 4
$p_1$ = 50 μHg
$\psi = \int_0^X \frac{\rho}{\rho_2} dX$
$1/\tau_2$ = 160
140
100
80
65
50
35
25
20
15
12.5
10
7.5
5
4
3.5
3
2.5
$\frac{\rho - \rho_1}{\rho_5 - \rho_1}$
3.0
2.0
1.0
0
10
20
30
40
50
60
$\psi$

Figure 18

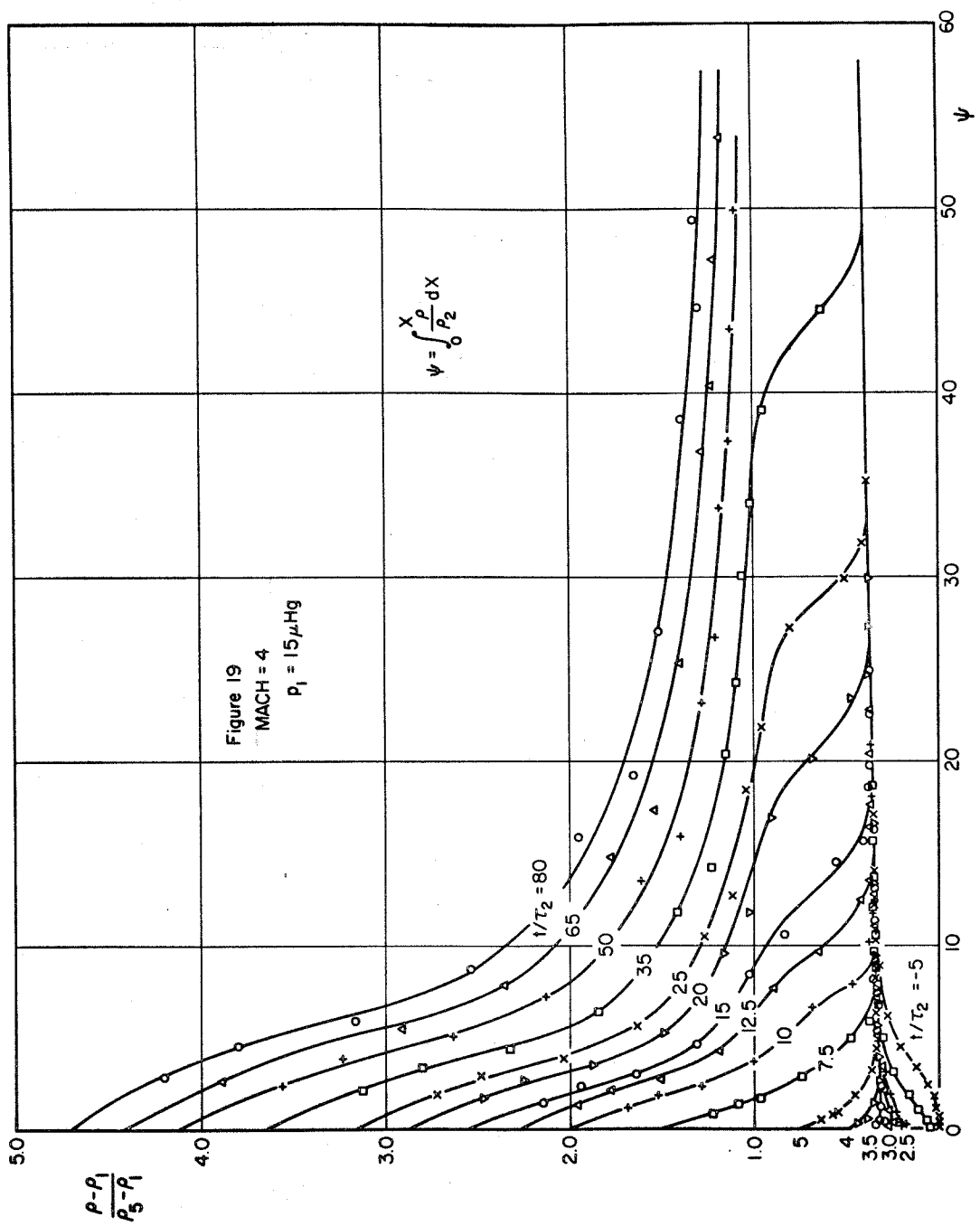
Figure 19
MACH = 4
$p_1$ = 15 μHg
$\psi = \int_0^X \frac{\rho}{\rho_2} dX$
$\frac{\rho - \rho_1}{\rho_5 - \rho_1}$
$t/\tau_2$ = 80
65
50
35
25
20
15
12.5
10
7.5
5
4
3.5
3.0
2.5
$t/\tau_2$ = -5
5.0
4.0
3.0
2.0
1.0
0
10
20
30
40
50
60
ψ

FIG. 19

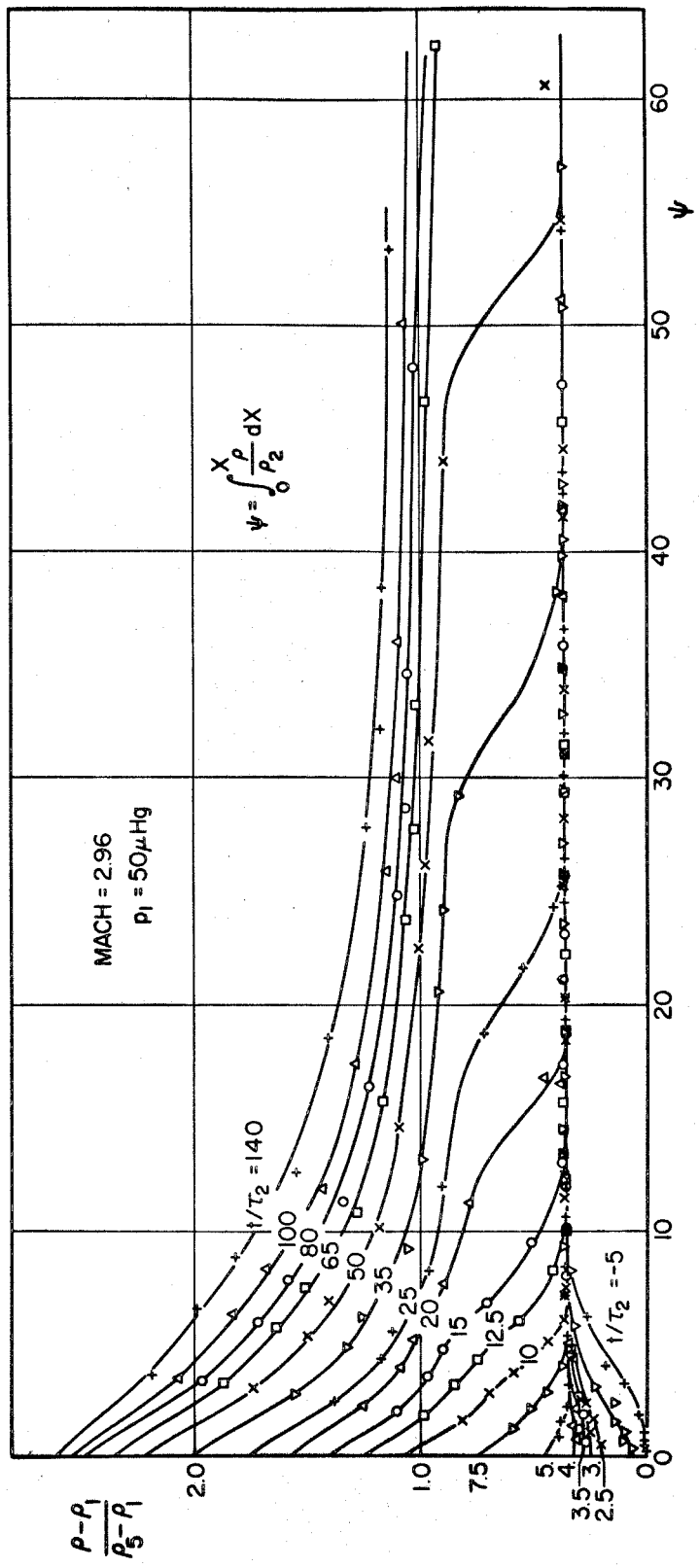
MACH = 2.96
p1 = 50μHg
$\psi = \int_0^X \frac{\rho}{\rho_2} dX$
$\frac{\rho - \rho_1}{\rho_2 - \rho_1}$
ψ
1/τ2 = 140
100
80
65
50
35
25
20
15
12.5
10
1/τ2 = -5
2.0
1.0
7.5
5
4
3.5
3
2.5
0
10
20
30
40
50
60

Figure 20

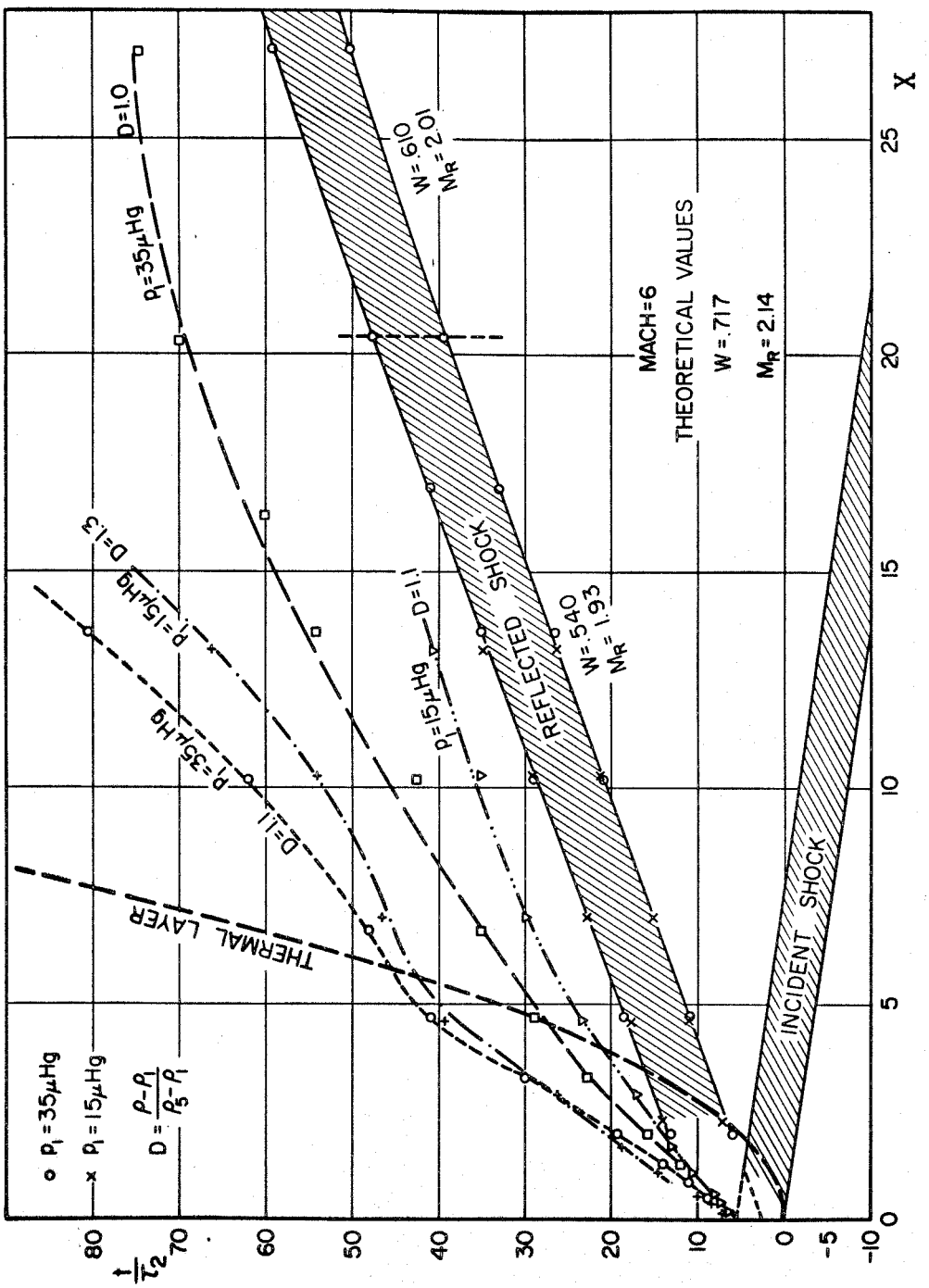


Figure 21 x-t DIAGRAM-EXPERIMENTAL

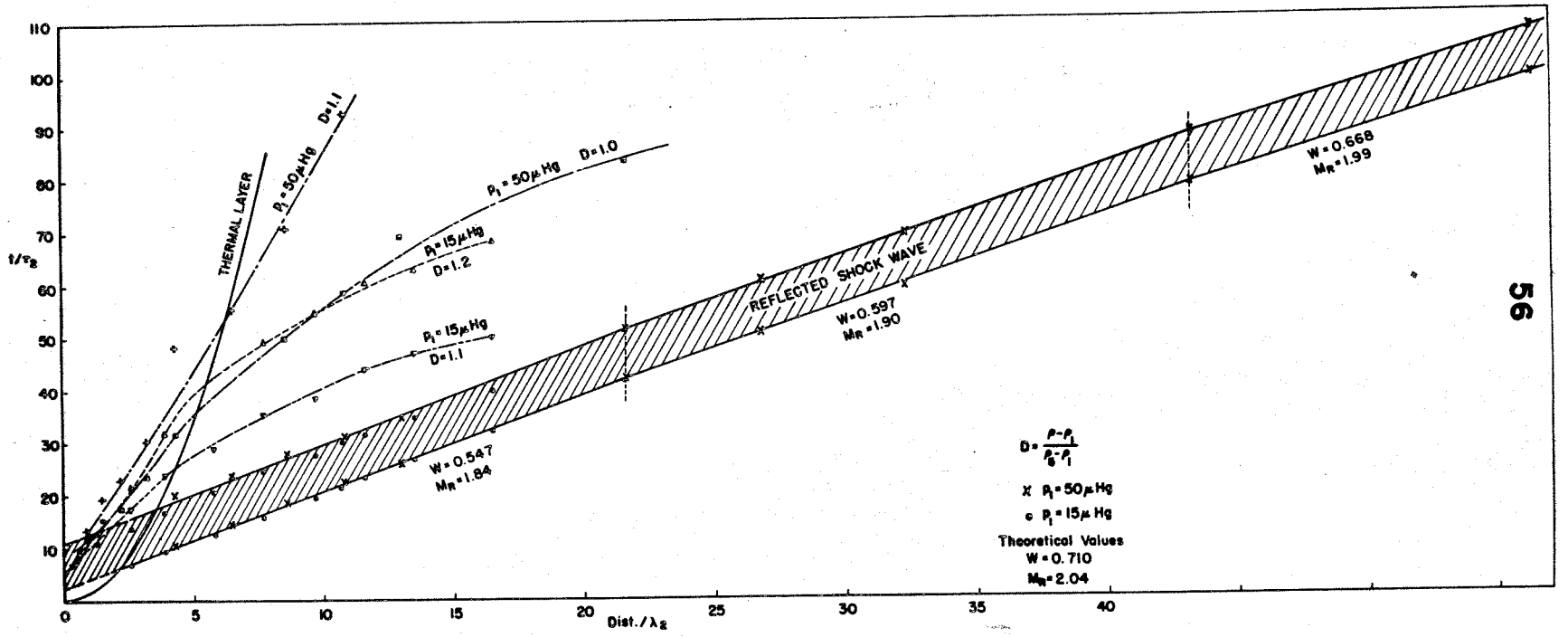


X – t DIAGRAM (EXPERIMENTAL, MACH = 4)

FIGURE 22

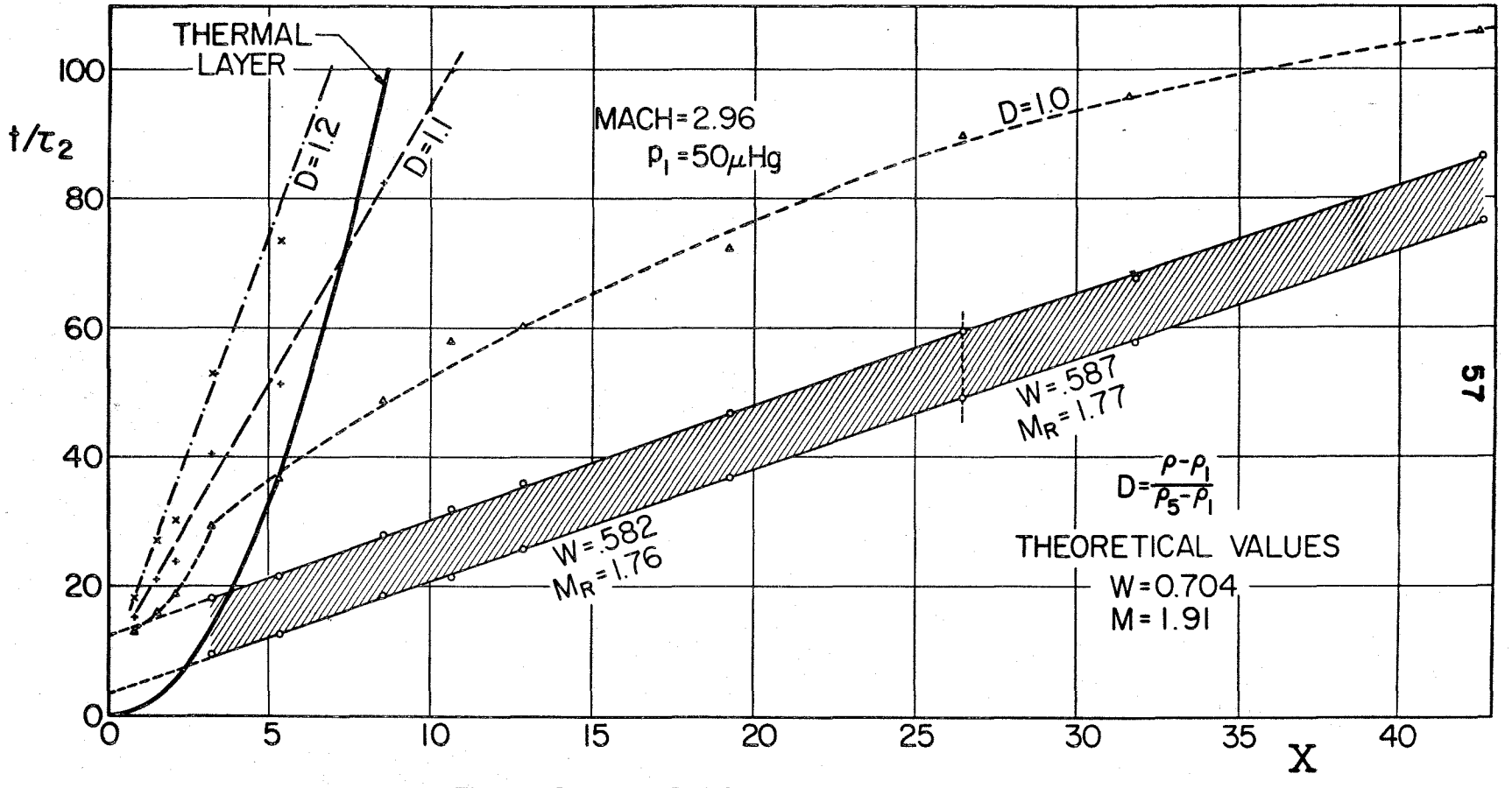


Figure 23 x-t DIAGRAM-EXPERIMENTAL

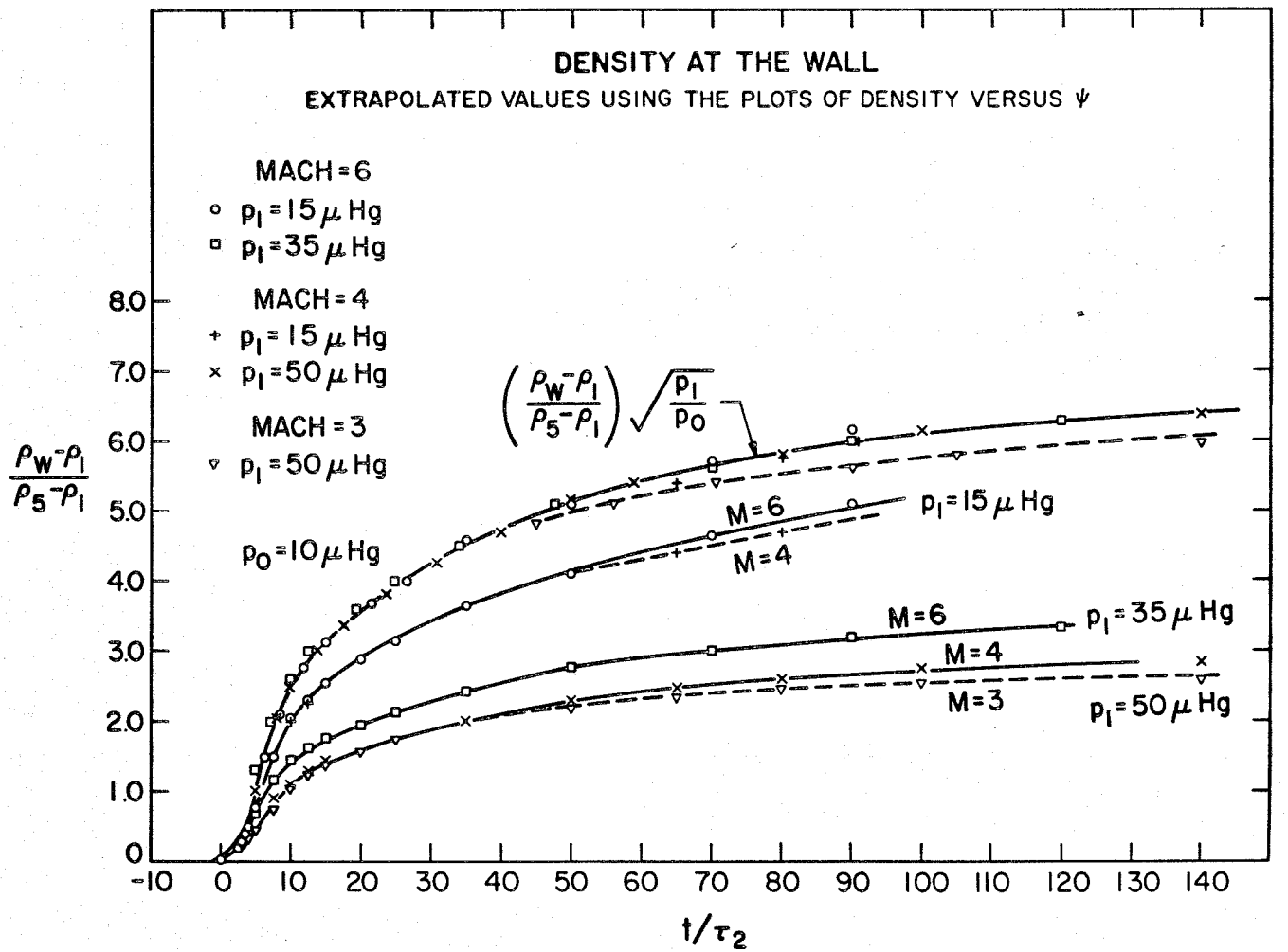
DENSITY AT THE WALL
EXTRAPOLATED VALUES USING THE PLOTS OF DENSITY VERSUS ψ
MACH = 6
p1 = 15 μ Hg
p1 = 35 μ Hg
MACH = 4
p1 = 15 μ Hg
p1 = 50 μ Hg
MACH = 3
p1 = 50 μ Hg
p0 = 10 μ Hg
(ρw − ρ1)/(ρ5 − ρ1) √(p1/p0)
M = 6
p1 = 15 μ Hg
M = 4
M = 6
p1 = 35 μ Hg
M = 4
M = 3
p1 = 50 μ Hg
(ρw − ρ1)/(ρ5 − ρ1)
8.0
7.0
6.0
5.0
4.0
3.0
2.0
1.0
0
-10
0
10
20
30
40
50
60
70
80
90
100
110
120
130
140
t/τ2

FIGURE 24

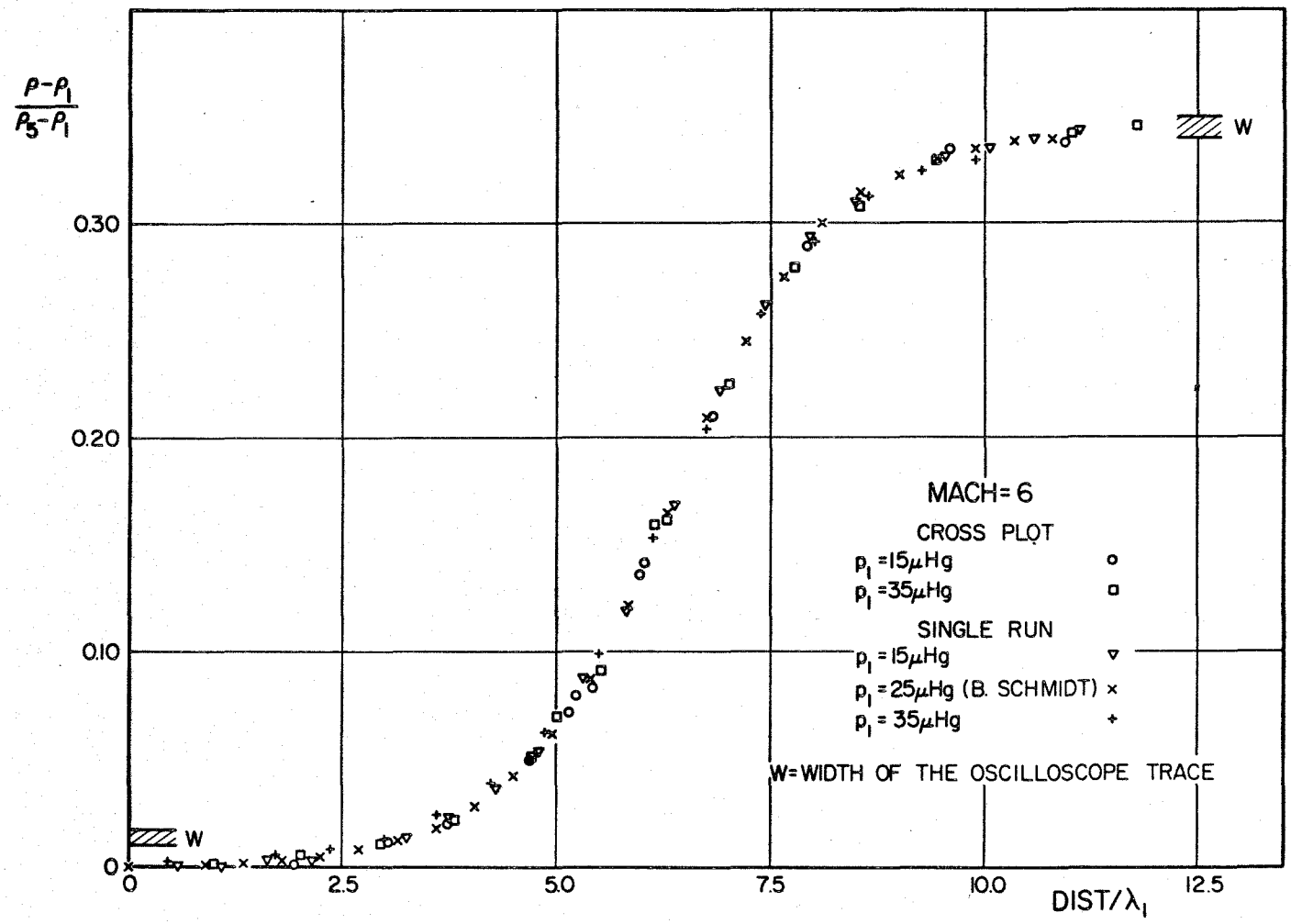


Figure 25 DENSITY PROFILE OF THE INCIDENT SHOCK WAVE

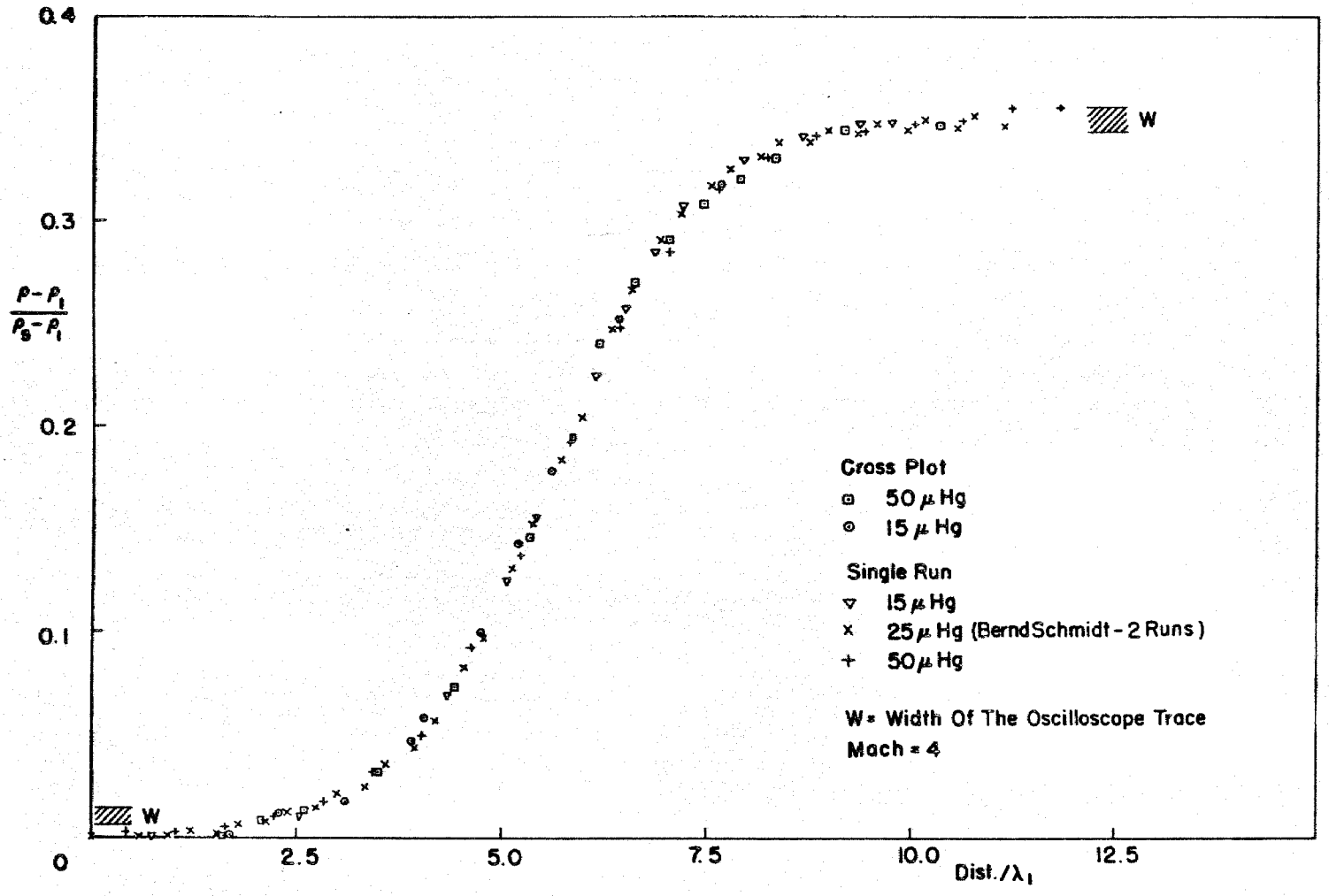


DENSITY PROFILES OF THE INCIDENT SHOCK WAVE

**Figure 26**

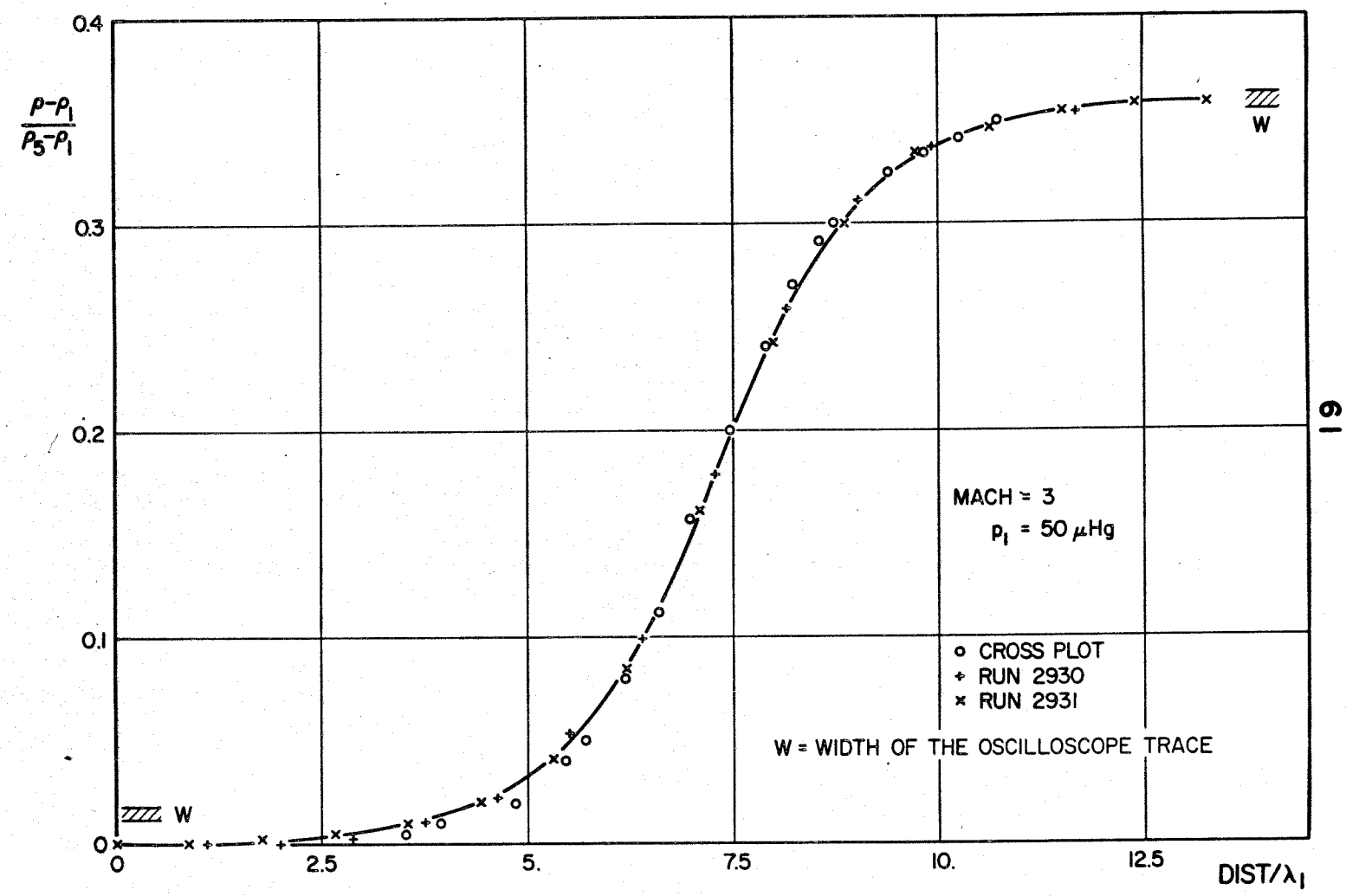


Figure 27 DENSITY PROFILE OF THE INCIDENT SHOCK WAVE